To appear in ApJ
Preprint typeset using LaTeX style emulateapj v. 25/04/01

NMA CO(J =1-0) OBSERVATIONS OF Hα/RADIO LOBE GALAXY NGC 3079: GAS DYNAMICS IN WEAK BAR POTENTIAL AND CENTRAL MASSIVE CORE

Koda, J.[1,2], Sofue, Y.[2], Kohno, K.[2], Nakanishi, H.[2], Onodera, S.[2], Okumura, S. K.[3], and Judith A. Irwin[4]

To appear in ApJ

ABSTRACT

We present our CO(1-0) observations in the central 4.5 kpc(1′) of Hα/Radio lobe galaxy NGC 3079 with the Nobeyama Millimeter Array. Molecular gas shows four remarkable components: a main disk, spiral arms, nuclear disk, and nuclear core. The main disk extends along the galaxy major axis. We detected its central 2 kpc in radius, while its full extent is beyond our spatial coverage. Molecular gas is smoothly distributed on the main disk, having gas mass of $5 \times 10^9 M_\odot$ within the central ~ 2 kpc radius. The spiral arms are superimposed on the main disk, forming a Z-shaped pattern on the sky. Abrupt velocity change of up to $\sim 200\,\mathrm{km\,s^{-1}}$ is observed along the spiral arms in S-shaped twists of isovelocity contours and double velocity-peak features on spectra. The nuclear disk with ~ 600 pc radius appears in position-velocity (PV) diagrams, having an intense concentration of molecular gas. Its appearances on PV diagrams are indicative of oval motions of the gas, rather than circular. The nuclear disk and spiral arms form the so-called "figure-of-eight" pattern on a PV diagram, which is sometimes found in edge-on barred galaxies. The nuclear core is more compact than our current resolution ($2'' = 150$ pc), having gas mass of $3 \times 10^8 M_\odot$ within the central 150 pc. Though it is unresolved with our resolution, the nuclear core shows a very high velocity $\sim 200\,\mathrm{km\,s^{-1}}$ even at the radius of ~ 100 pc on the PV diagram.

A weak bar model successfully explains the observed features of the main disk, spiral arms, and nuclear disk. The main disk and spiral arms result from gaseous x_1-orbits and their crowdings respectively. The nuclear disk arises from gaseous x_2-orbits. The gas concentration on the nuclear disk is also explained by fueling mechanism; the gas on x_1-orbits flows along spiral arms (or offset shocks), colliding with the gas on x_2-orbits, and accumulating onto the nuclear disk. Assuming that the gas moves along the spiral arms which run perpendicular to the line-of-sight, the pattern speed of bar is estimated to be $55 \pm 10\,\mathrm{km\,s^{-1}\,kpc^{-1}}$. However rapidly rotating nuclear core is out of our model for a bar, and any orbit caused by a bar is not likely to produce that high velocity. Thus we attribute the high velocity to a central massive core with dynamical mass of $10^9 M_\odot$ within the central 100 pc. This mass is three orders of magnitude more massive than that of a central black hole in this galaxy. This is the first clear evidence for the presence of central massive core.

Subject headings: galaxies: active — galaxies: ISM — galaxies: kinematics and dynamics — galaxies: spiral — galaxies: structure

1. INTRODUCTION

NGC 3079 is a nearly edge-on ($i = 77°$) SBc galaxy at a distance of 15.6 Mpc (1 arcsec corresponds to 76 pc; Sofue et al. 1999). Its nucleus is classified as LINER (Heckman 1980) or Seyfert 2 (Ford et al. 1986; Sosa-Brito, Tacconi-Garman & Lehnert 2001) from optical emission spectrum, and shows strong H_2O maser emission (Henkel et al. 1984; Trotter et al. 1998). Overall velocity distribution of H_2O masers suggests the presence of a binding mass of $\sim 10^6 M_\odot$ at the center (Trotter et al. 1998), possibly a central supermassive black hole, which has been found in many AGNs (Miyoshi et al. 1995; Wandel, Peterson & Malkan 1999; Ishihara et al. 2001). Persec-scale nuclear jets observed in radio continuum may be outflow from the central compact object (Irwin & Seaquist 1988; Sawada-Satoh et al. 2000).

EDITOR: PLACE FIGURE 1 HERE.

Kilopersec-scale significant outflow along the galaxy minor axis is observed as lobes in radio continuum (Duric & Seaquist 1988), Hα emission (Ford et al. 1986; Veilleux et al. 1994; Cecil et al. 2001, see Figure 1), and X-ray emission (Fabbiano, Kim & Trinchieri 1992; Pietcsh, Trinchieri & Vogler 1998). An optical spectroscopy shows gas motions with a velocity range of $\sim 2000\,\mathrm{km\,s^{-1}}$ across the lobes, and unusually high [N II]/Hα line ratios which indicate the presence of shocks (Veilleux et al. 1994). This type of large-scale outflow is often attributed to starburst activity (Heckman, Armus & Miley 1990). However there are some arguments against this starburst model for NGC 3079 (Hawarden et al. 1995). Duric & Seaquist (1988) presents an alternative model that a wind flow from the nucleus could be directed toward the galaxy minor axis by interaction with dense gas surrounding the nucleus. This interaction produces shocks which explain observed strength of H_2 emission from lower vibration transitions by collisional excitation (Hawarden et al. 1995).

[1] JSPS Research Fellow; E-mail: koda@ioa.s.u-tokyo.ac.jp
[2] Institute of Astronomy, University of Tokyo, Mitaka, Tokyo 181-0015, Japan
[3] Nobeyama Radio Observatory, Minamisaku, Nagano, 384-1305, Japan
[4] Department of Physics, Queen's University, Kingston, ONK7L3N6, Canada

At the root of the kilopersec-scale outflow, there is a dense molecular disk with a radius of a few kilopersec (Young, Claussen & Scoville 1988; Sofue & Irwin 1992; Irwin & Sofue 1992; Sofue et al. 2001). Based on their interferometry observations of CO($J = 1 - 0$) emission, Sofue & Irwin (1992) found the intense concentration of gas on the molecular disk, spiral arm features appearing on a position-velocity diagram, and the existence of a central compact core which was unresolved in their resolution ($4''$). Sofue et al. (2001) have confirmed these features, and further resolved and classified the innermost region as the nuclear molecular disk and ultra high density core, based on their appearances on intensity maps and position-velocity diagrams. [In this paper, we will re-classify the features based on the data including new observations (§3) and on theoretical considerations (§4).] The molecular disk was also observed in the emissions of HCN and HCO^+ (Kohno et al. 2001).

The disk of NGC 3079 is rotating with north-side approaching and south-side receding. A K'-band image shows spiral arms on the disk, forming a Z-shaped pattern on the sky (Veilleux, Bland-Hawthorn & Cecil 1999). If trailing spiral arms are assumed, the west of NGC 3079 is near-side, which is consistent with the entire dust lane morphology. NGC 3079 is one of far-infrared (FIR) luminous galaxies listed in the *IRAS* bright galaxy catalog (Soifer et al. 1989). An *ISO* $90\mu m$ map shows that most of the FIR emission is produced by dust heated by stars in the entire galaxy disk, rather than the nucleus (Pérez García, Rodríguez Espinosa & Fuensalida 2000). The HI disk extends more widely than the optical disk and shows warps at the outskirts (Irwin & Seaquist 1991). These warps may originate from an interaction with a nearby companion NGC 3073. The HI velocity field, however, shows a regular pattern of rotating disk. The radial emission profile is well fitted by an exponential function, while it shows a sharp drop in the central region ($< 50''$; Irwin & Seaquist 1991) which is produced by absorption against strong continuum emission (Duric & Seaquist 1988). The CO disk is embedded in this region of the absorbed HI (Young, Claussen & Scoville 1988; Sofue & Irwin 1992; Sofue et al. 1999), and coincident with a void of Hα line emission (Cecil et al. 2001).

Though NGC 3079 is classified as a barred galaxy (SBc), the stellar bar is hardly confirmed in optical/infrared photographs in this nearly edge-on galaxy. There are however some evidence for the presence of a bar. NGC 3079 has a stellar bulge which takes a so-called peanuts-shape (Shaw, Wilkinson & Carter 1993), whose possible origin is a vertical instability of rotating disk-stars in a bar potential (Combes et al. 1990). Veilleux, Bland-Hawthorn & Cecil (1999) fitted an oval orbit model to their Hα velocity field, and concluded that bar streaming motions with moderately eccentric orbits ($e = b/a \sim 0.7$) aligned along P.A. = 163° on the sky [5] (P.A. = 130° intrinsic to the disk) are satisfactory to match the observations.

In this paper, we present our recent CO(J =1-0) observations of the central $1'$ of NGC 3079 using the Nobeyama Millimeter Array (NMA). We describe our observations and data analysis in §2. A part of the data has been published in Sofue et al. (2001), but this paper presents our new analysis including new observations. Main features in the molecular disk of NGC 3079 are presented in §3. Gas dynamics on the molecular disk is discussed in §4. A weak bar and central massive core successfully explain all observed features. Central rotation curve and mass are derived in §5. We summarize our conclusions in §6.

2. OBSERVATIONAL DATA

2.1. *NMA CO(J =1-0) Observations*

Our aperture synthesis observations of the CO(J =1-0) emission from NGC 3079 were obtained with the Nobeyama Millimeter Array (NMA) at the Nobeyama Radio Observatory (NRO) [6], between 2000 January and 2001 April for a single pointing center at (α_{1950}, δ_{1950}) = ($9^{\rm h}58^{\rm m}35^{\rm s}.02$, $+55°55'15''.40$). We made the observations with three available configurations (AB, C, and D); when combined, the visibility data cover projected baselines from 10.4 to 351 m. The NMA consists of six 10 m antennas, providing the FWHP of about $65''$ at 115 GHz. The antenna size limits the minimum projected baseline, restricting the largest detectable size of objects to about $54''$. Tunerless SIS receivers at the front-end have receiver noise temperatures of about 30 K in double sidebands, and typical system noise temperatures of about 400 K in single sidebands. Digital spectro-correlators (Okumura et al. 2000) at the back-end have two spectroscopic modes; we used a mode covering 512 MHz ($1331\,{\rm km\,s^{-1}}$) with 2 MHz ($5.2\,{\rm km\,s^{-1}}$) resolutions. We observed the quasar 0954+556 every 20 minutes for gain calibration, and 3C279 (or 3C273) for bandpass calibration. Absolute flux scales (0.68 Jy at 115 GHz for 0954+556, uncertain to $\sim 20\%$) were measured three times in 2000 and once in 2001; no significant flux variation was observed.

The raw visibility data were calibrated for complex gain and passband with the UVPROC-II package developed at NRO, and mapped with the NRAO/AIPS package. We applied the CLEAN procedure with natural weighting for each velocity channel, and obtained a three-dimensional (RA, DEC, $V_{\rm LSR}$) data cube. Parameters of the cube are listed in Table 2.

EDITOR: PLACE TABLE 2 HERE.

Figure 2 displays zeroth- and first-moment maps in the central $48'' \times 20''$ region ($3.7\,{\rm kpc} \times 1.5\,{\rm kpc}$) of NGC 3079, while Figure 3 shows channel maps with an interval of $10.4\,{\rm km\,s^{-1}}$ in the same region. The significant emission ($> 3\sigma$; $1\sigma = 12\,{\rm mJy\,beam^{-1}}$) is detected in adjacent 63 channels within the velocity range of $V_{\rm LSR} = 821 - 1467\,{\rm km\,s^{-1}}$ ($\Delta V = 646\,{\rm km\,s^{-1}}$). No primary beam correction has been applied in these maps. Figure 4 displays a position-velocity diagram (PV diagram) along the optically defined major axis (P.A.= 165°), integrated along the minor axis. The almost entire CO emission in Figure 2 (*left*) falls in the slit-width ($12''$). The axes are labeled relative to the dynamical center, and systemic recession velocity of the galaxy (derived in § 3.1.2; see Table 3).

[5] This value is calculated by $\tan({\rm P.A.}_{\rm gal} - {\rm P.A.}_{\rm sky}) = \tan({\rm P.A.}_{\rm gal} - {\rm P.A.}_{\rm int}) \cdot \cos i$

[6] Nobeyama Radio Observatory is a branch of the National Astronomical Observatory, operated by the Ministry of Education, Culture, Sports, Science and Technology, Japan.

EDITOR: PLACE FIGURE 2 HERE.

EDITOR: PLACE FIGURE 3 HERE.

EDITOR: PLACE FIGURE 4 HERE.

Figure 5 compares spectra from our NMA cube with those of single-dish observations from IRAM 30 m and FCRAO 14 m telescopes (Braine et al. 1993; Young et al. 1995). In order to obtain the spectra comparable to the single-dish ones, the NMA cube was corrected for the primary beam response of antennas, convolved with the single-dish beam (23″ for IRAM and 45″ for FCRAO), and sampled at the pointing center of the single-dish observations. The full width of zeroth velocity of the NMA spectrum is almost the same as that of IRAM, but different from that of FCRAO. The emission around $V_{\rm LSR} \sim 800\,{\rm km\,s^{-1}}$ in the FCRAO spectrum may be spatially too extended to be detected in our interferometric observations; a similar emission feature was seen at the 45″ northwest side in FCRAO observations (Young et al. 1995). The NMA cube recovers about 87% of the total CO line flux in the central 23″ while 67% in 45″, which means that the CO emission is concentrated in the central region. We made no correction for the missing flux in the following discussions.

EDITOR: PLACE FIGURE 5 HERE.

2.2. *Supplied HST Data*

We obtained images from the *Hubble Space Telescope (HST)* archive (P.I. G. Cecil; see Cecil et al. 2001). The images were taken with WFPC2 and two filters, F814W and F658N, which correspond to the I-band and Hα+[N II] filters in ground telescopes. The central part of NGC 3079 lies on a WFC chip rather than the PC chip. Cosmic-ray hits were removed and images are combined with the IRAF/STSDAS package. The absolute position of the *HST* images is calibrated using the USNO-A2.0 catalog (Zacharias et al. 2000), and is accurate to about 0″.5. The derived images are presented in the right-hand panel of Figure 1.

3. RESULTS

Our maps and PV diagram show four distinct components: a main disk, spiral arms (or offset ridges), a nuclear disk, and a nuclear core. Figure 6 shows a schematic illustration of these four components on a PV diagram. We describe each of the four in order of decreasing radius in §3.1-3.4, and compare them with previous results in §3.5.

EDITOR: PLACE FIGURE 6 HERE.

3.1. *The Main Disk*

3.1.1. *Smooth Gas Distribution on the Main Disk*

The zeroth-moment map of Figure 2 displays a disk with an extent of 45″ × 15″ (3.4 kpc × 1.1 kpc), elongated along the optically-defined major axis of the galaxy (P.A. = 165°). Since our synthesis observations has an intrinsic maximum limit of detectable scale (54″), larger components detected in single-dish observations [7] are not covered in this map, and result in the missing flux (our total flux recovery is about 67% in 45″). The inclination of the galaxy (77°) is large, but enough to show the emission distribution on the disk, because the vertical sizes of molecular disks are usually thin (150 pc for the Galaxy from Clemens, Sanders & Scoville 1988; 230 pc for NGC 891 from Handa et al. 1992) in comparison with the full extents of molecular disks (3.4 kpc or 45″ for NGC 3079 from the zeroth-moment map). The CO emission is smoothly distributed on the full disk, showing no emission deficient regions often found in molecular disks (see Sakamoto et al. 1999a; Regan et al. 2001). The emission distribution is nearly axisymmetric, except slight enhancements owing to spiral arms (see § 3.2) which run northwest and southeast from the galaxy center. The main disk coincides with the void of HII regions (Cecil et al. 2001, see also Figure 7 *left*), and with the region where the HI gas is observed in absorption (Irwin & Seaquist 1991) against strong radio continuum emission (Duric & Seaquist 1988). The center of the main disk is coincident well with the root of the Hα-lobe.

EDITOR: PLACE FIGURE 7 HERE.

3.1.2. *Kinematics of The Main Disk*

The first-moment map (Figure 2 *right*) shows a rotating disk with the northside approaching and southside receding. The S-shaped twists of isovelocity contours are coincident with spiral arms, and evidence non-circular motions (§ 3.2). The entire velocity field is almost perfectly bisymmetric, indicating regular motions in the molecular disk.

We obtained kinematical parameters from the first-moment map using the AIPS/GAL package. The dynamical center, position angle and inclination are first determined using the Brandt rotation curve model (Brandt 1965). Then we fixed the above parameters, fitted tilted ring models with constant velocities to the first-moment map, and obtained the systemic recession velocity (LSR velocity). The results are listed in Table 3. The dynamical center coincides spatially with the emission centroid: $(\alpha_{1950}, \delta_{1950}) = (09^{\rm h}58^{\rm m}35^{\rm s}.00, +55^{\rm d}55^{\rm m}15^{\rm s}.80)$. The position angle and inclination are in good agreement with the results from optical isophotes (Sandage & Tamman 1981; Veilleux, Bland-Hawthorn & Cecil 1999) and from kinematics of the HI gas (Irwin & Seaquist 1991). The systemic recession velocity is consistent with estimates from optical spectroscopic data (e.g. 1150 km s^{-1} from Veilleux, Bland-Hawthorn & Cecil 1999), but slightly exceeds the value from HI data (1124 km s^{-1} from Irwin & Seaquist 1991). This difference might come from a warp of the

[7] Recently, NRO 45 m telescope observations found that the full extent of CO emission in NGC 3079 is about 80 ″ in radius (Yamauchi, private communication).

HI disk (Irwin & Seaquist 1991). We adopt the values from large-scale isophotos for position angle and inclination, and the derived values for galaxy center and systemic recession velocity in the rest of our analysis.

EDITOR: PLACE TABLE 3 HERE.

The PV diagram (Figure 4) shows the main disk as two ridges, symmetrically extending southeast and northwest from the velocity peaks around the center (see also Figure 6). The near-perfect symmetry in the diagram again indicates regular motions of the molecular gas in the disk. The velocity of $220\,\mathrm{km\,s^{-1}}$ at the radius of $26''$ (2.0 kpc) indicates the dynamical mass of $M_{\rm dyn} = 2.2 \times 10^{10} M_\odot$. The disk is also confirmed in the channel maps (Figure 3); the approaching (NW) side appears in the channels of $V_{\rm LSR} = 821 - 1029\,\mathrm{km\,s^{-1}}$, while the receding (SE) side is found in $V_{\rm LSR} = 1258 - 1467\,\mathrm{km\,s^{-1}}$.

3.1.3. *Mass and Surface Densities of the Molecular Gas*

Masses of molecular gas $M_{\rm H_2}$ are estimated from total CO-line flux $S_{\rm CO}$, CO-to-H_2 conversion factor $X_{\rm CO}$, and galaxy distance D by

$$\left(\frac{M_{\rm H_2}}{M_\odot}\right) = 7.2\times10^3 \left(\frac{D}{\rm Mpc}\right)^2 \left(\frac{S_{\rm CO}}{\rm Jy\,km\,s^{-1}}\right) \times \left(\frac{X_{\rm CO}}{1.8\times10^{20}{\rm cm^{-2}\,[K\,km\,s^{-1}]^{-1}}}\right). \quad (1)$$

Assuming the hydrogen mass fraction (0.707 from Cox et al. 2000), the total gas mass, including He and other elements, becomes $M_{\rm gas} = 1.41 M_{\rm H_2}$. Face-on surface densities of molecular gas are calculated from integrated CO line intensity $I_{\rm CO}\Delta V$, galaxy inclination i, and conversion factor $X_{\rm CO}$ by

$$\left(\frac{\Sigma_{\rm H_2}}{M_\odot\,{\rm pc^{-2}}}\right) = 3.0\times10^2 \cos i \left(\frac{I_{\rm CO}\Delta V}{\rm Jy\,km\,s^{-1}\,arcsec^{-2}}\right) \times \left(\frac{X_{\rm CO}}{1.8\times10^{20}{\rm cm^{-2}\,[K\,km\,s^{-1}]^{-1}}}\right). \quad (2)$$

The surface densities of total gas also becomes $\Sigma_{\rm gas} = 1.41\Sigma_{\rm H_2}$. The surface density estimation is independent of galaxy distances. We adopt the conversion factor of $X_{\rm CO} = 1.8\times10^{20}{\rm cm^{-2}\,[K\,km\,s^{-1}]^{-1}}$ from observations in the Galaxy (Dame, Hartmann and Thaddeus 2001), while $X_{\rm CO}$ could be smaller in galactic center regions (Arimoto, Sofue and Tsujimoto 1996).

The total flux within the radius of $26''$ is $S_{\rm CO} = 1.9\times10^3\,\mathrm{Jy\,km\,s^{-1}}$, which corresponds to $M_{\rm gas} = 4.6\times10^9 M_\odot$ for the galaxy distance $D = 15.6\,$Mpc. The ratio of dynamical mass ($2.2\times10^{10} M_\odot$ from §3.1.2) to the total molecular gas mass $M_{\rm gas}/M_{\rm dyn}$ is about 21% within the radius of 2 kpc. The peak integrated intensity is $I_{\rm CO}\Delta V = 1.3\times10^2\,\mathrm{Jy\,beam^{-1}\,km\,s^{-1}}$ (or $3.8\times10^3\,\mathrm{K\,km\,s^{-1}}$) at ($\alpha_{1950}$, δ_{1950}) = ($09^{\rm h}58^{\rm m}35^{\rm s}.00$, $+55^\circ55'15''.80$); the corresponding face-on surface density becomes $\Sigma_{\rm gas} = 2.5\times10^3 M_\odot\,{\rm pc^{-2}}$. No correction for missing flux is applied.

Figure 8 shows the radial profile of the CO emission. Integrated intensities are azimuthally averaged in each annulus ($\Delta r = 0.5''$) with corrections for inclination (77°) and primary beam attenuation. The outskirts of the profile ($r > 5''$) is well fitted by an exponential (dotted line). At the innermost region, the CO emission exceeds this exponential curve, indicating a high CO concentration at the central region. Surface densities of molecular gas are labeled at the right-hand axis. The observed value of $\Sigma_{\rm H_2} = 1000\,M_\odot{\rm pc^{-2}}$ at $r \sim 5''$ (380 pc) is an order of magnitude higher than the typical value for the central regions of nearby galaxies (Sakamoto et al. 1999b).

EDITOR: PLACE FIGURE 8 HERE.

The HI gas surface density also follows an exponential profile $\Sigma^0_{\rm HI}\, e^{-r/h_{\rm HI}}$ where $h_{\rm HI} = 118''$ (9.0 kpc) and $\Sigma^0_{\rm HI} = 8.8\times10\,M_\odot\,{\rm pc^{-2}}$ (Irwin & Seaquist 1991, from their Table 4). In comparison with this HI profile, our H_2 profile (dotted line) takes the same surface density at nearly the edge of our detected molecular disk ($r \sim 23''$ or 1.7 kpc), rising more steeply toward the galaxy center ($h_{\rm CO} \sim 7.2''$ or 550 pc). This indicates that the gas in NGC 3079 is highly concentrated in the the central molecular disk.

3.2. *The Spiral Arms/Offset Ridges*

The zeroth-moment map (Figure 2 *left*) shows arm-like enhancements of emission, superimposed on the main disk; two ridges bisymmetrically run northwest and southeast from the galaxy center, forming a Z-shaped pattern. These features resemble spiral arms, or offset ridges often found at the leading edge of stellar bars. If the west of the galaxy is at the near-side as suggested by dust lane morphology, the arms are trailing. The S-shaped twists of isovelocity contours on the first-moment map (Figure 2 *left*) coincide with the two arms, indicating non-circular motions around the spiral arms. Similar counterclockwise spiral arms have been found in a K'-band image (Veilleux, Bland-Hawthorn & Cecil 1999).

Figure 9 shows line-profiles of CO emission at 5×7 points on a $3''$-spacing grid (crosses on the left-hand panel), centered at the dynamical center (Table 3). Remarkable double-peak features appear along the spiral arms: arrows point examples of the double-peaks. The northwest arm corresponds to the peaks with higher velocities, while the southeast arm does to the peaks with lower velocities. The other peaks come from the main disk. These distinct velocities between the main disk and spiral arms (typically $\Delta V \sim 200\,\mathrm{km\,s^{-1}}$) produce the S-shaped twists in the first-moment map. Similar double-peak features have been noticed from Hα-spectroscopic data (Filippenko & Sargent 1992; Veilleux, Bland-Hawthorn & Cecil 1999), though their low velocity resolutions did not allow to distinguish between the main disk and spiral arms.

EDITOR: PLACE FIGURE 9 HERE.

The spiral arms are also confirmed on the PV diagram (Figure 4; see also Figure 6). Two ridges run northwest and southeast with lower velocities than those of the main disk. These two ridges and a central ridge of the nuclear disk (§3.3) show a so-called "figure-of-eight" pattern (or "tilted X" pattern) often found in barred galaxies (Handa et al. 1990; Laine et al. 1990; Merrifield & Kuijken 1999). In the velocity range of $\Delta V = \pm150\,\mathrm{km\,s^{-1}}$ ($V_{\rm sys} = 1147\,\mathrm{km\,s^{-1}}$), the spiral arms are more dominated in emission than the main disk. This is also evident in

the channel maps (Figure 3). The spiral arms are clearly confirmed at $V = 1010 - 1280\,\mathrm{km\,s^{-1}}$; emission from the northwest and southeast arms appear at the northwest and southeast edges of maps at 1010 and $1280\,\mathrm{km\,s^{-1}}$, approaching the innermost core with increasing and decreasing velocities, respectively. Figure 7 (right-hand panel) shows contours of a zeroth-moment map made in the velocity range of $\Delta V \pm 100\,\mathrm{km\,s^{-1}}$ centered at the systemic recession velocity (superimposed on the Hα + [N II] map). The spiral arms is rooted to the nucleus, winding counterclockwise.

3.3. *The Nuclear Disk*

The nuclear disk shows a sign of an existence on the PV diagram (Figure 4): remarkable velocity-peaks appear symmetrically at ($-7''$, $+250\,\mathrm{km\,s^{-1}}$) and ($+7''$, $-250\,\mathrm{km\,s^{-1}}$). Figure 10 shows PV diagrams with $1''$-width and offsets of $+2''$, $0''$ and $-2''$ along the galaxy minor axis. The cuts are along the galaxy major axis. These diagrams reveal that the two peaks are on a single kinematical sequence: ridges are runing and connecting the two peaks through three panels (see also Figure 6). This sequence seems to be rotating in this innermost region and forming a nuclear disk. The nuclear disk is obviously distinct from other velocity-peaks at the innermost region (at $\pm 1''$ in Figure 4), because their corresponding peaks appear only in the diagram with $0''$-offset; we thus think they are consequences of the nuclear core (see § 3.4). The very high CO concentration within the nuclear disk ($r < 7''$; Figure 4 and 8) indicates its distinct nature from the main disk. We conclude that the component which appears as the peaks and ridges in the PV diagrams is the nuclear disk. This component is rotating around the galaxy center with the northside approaching and southside receding.

EDITOR: PLACE FIGURE 10 HERE.

In the three panels of Figure 10, the ridges corresponding to the nuclear disk are not on a straight line connecting their two velocity peaks: the ridges are bent downward and upward in the $+2''$ and $-2''$ offset diagrams respectively, while it twists upward (at the left-hand side) and downward (right-hand side) in the $0''$-offset diagram. Beyond the appearances, the deviations from the straight line amount up to $\sim 50\,\mathrm{km\,s^{-1}}$. These symmetrical bends and twist indicate that the gas in the nuclear disk takes oval orbits rather than circular (see § 4).

The nuclear disk is also seen in the channel maps (Figure 3). The two velocity-peaks on the PV diagrams appears in the channels of $V_{\mathrm{LSR}} = 822 - 926\,\mathrm{km\,s^{-1}}$ as an emission peak at around $7''$-north from the center, and in $V_{\mathrm{LSR}} = 1384 - 1467\,\mathrm{km\,s^{-1}}$ at around $7''$-south. In other channels, strong emission from the main disk and nuclear core contaminates and removes that from the nuclear disk.

3.4. *The Nuclear Core*

The nuclear core is most clearly seen in the PV diagram (Figure 4), which appears as two velocity-peaks at ($-1''$, $+240\,\mathrm{km\,s^{-1}}$) and ($+1''$, $-240\,\mathrm{km\,s^{-1}}$). The distinct kinematics of this core from the other components is evident in a series of PV diagrams which have positional offsets along the galaxy minor axis (Figure 10). Among the three diagrams with $+2''$, $0''$ and $-2''$-offsets, the nuclear core appears only in the central one. The high velocities indicate a large dynamical mass in this nuclear region if the gas is pure-circularly rotating; we will discuss this in § 4.4.

The zeroth-moment map (Figure 2) shows the nuclear core as intense CO concentration at the very center of the galaxy. It is also confirmed in channel maps (Figure 3) in almost all the velocities ($V_{\mathrm{LSR}} = 863 - 1436\,\mathrm{km\,s^{-1}}$). The central gas density of the nuclear core is as high as $2.5 \times 10^3 M_\odot\ \mathrm{pc^{-2}}$, which is about an order of magnitude higher than the typical for nearby normal galaxies (Sakamoto et al. 1999a). This value is however a lower limit, because the core is unresolved even in our high resolution observations ($1.9'' \times 1.6''$), The total flux within the radius of $2''$ (152 pc) is $S_{\mathrm{CO}} = 1.2 \times 10^2\,\mathrm{Jy\,km\,s^{-1}}$; the corresponding gas mass is $M_{\mathrm{gas}} = 3.0 \times 10^8 M_\odot$.

3.5. *Comparison with Previous Results*

On the molecular disk of NGC 3079, Sofue & Irwin (1992) identified three main components: an outer disk, spiral arms, and a central compact core. Recently Sofue et al. (2001) further resolved the central compact core, and classified it into two distinct components, a nuclear molecular disk and ultra-high-density molecular core, based on their appearances on maps and PV diagrams. In this paper, we re-classified observed features into four distinct components, based on our new observations and analyses, and partly on theoretical considerations in §4. The outer disk and spiral arms in Sofue & Irwin (1992) correspond to our main disk and spiral arms respectively, and the ultra-high-density molecular core in Sofue et al. (2001) corresponds to our nuclear core. The nuclear molecular disk in Sofue et al. (2001) is different from our nuclear disk, and includes both our nuclear disk and main disk in part.

Though Sofue & Irwin (1992) reported an absorption feature in the spectrum at the galaxy center, we could not find such feature in our spectrum (Figure 5). This discrepancy may arise from their low resolution ($4''$) which could blend the central spectrum with the surrounding double-peak ones in Figure 5. The two peaks on a PV diagram at the central part, found by Sofue & Irwin (1992), is also confirmed in Figure 10. This feature however cannot be confidently attributed to the nuclear ring (Sofue & Irwin 1992) because the two peaks may arise from our nuclear disk (see Figure 10 *top* and *bottom*) superposed on our nuclear core. Our central surface density $\Sigma_{\mathrm{gas}} = 2.5 \times 10^3 M_\odot\ \mathrm{pc^{-2}}$ is consistent with the value ($2.2 \times 10^4 M_\odot\ \mathrm{pc^{-2}}$) of Sofue & Irwin (1992) by considering the difference of the adapted conversion factors and applying the correction for inclination to the value of Sofue & Irwin (1992). We could not find firm evidence for the nuclear molecular jet (Irwin & Sofue 1992) in our data.

4. GAS DYNAMICS IN NGC 3079

The near-perfect bisymmetric structures in the emission distribution and kinematics of the molecular disk are considerable. These kinds of bisymmetry are often thought to be consequences of gas motions under bar. Though a stellar bar is hardly certified from optical/infrared photos in this nearly edge-on galaxy, there are some observational evidence for the presence of a bar: the peanuts-shaped

bulge (Combes et al. 1990; Shaw, Wilkinson & Carter 1993); the "figure-of-eight" pattern on the PV diagram (Kuijken & Merrifield 1995); the high central concentration of the molecular gas (Sakamoto et al. 1999b); the Hα velocity field well-fitted by an oval-orbits model under a weak bar (Veilleux, Bland-Hawthorn & Cecil 1999). We thus propose a model that NGC 3079 contains a weak bar. This model naturally explain the features in § 3: the main disk and spiral arms (or offset ridges) may result from gaseous x_1-orbits and their crowdings respectively. The nuclear disk may arise from gaseous x_2-orbits. This model however cannot interpret the nuclear core, which necessitates a massive component besides the bar at the galaxy center. Figure 11 shows schematic views of our interpretation, overdrawn on our model orbits (in advance of detailed descriptions in §4.1). We present below our detailed cases for the existence of the weak bar, the origin of the main disk, spiral arms, nuclear disk and core.

EDITOR: PLACE FIGURE 11 HERE.

4.1. *Damped Orbit Model*

We adopt a damped orbit model by Wada (1994) and Sakamoto, Barker & Scoville (2000) to describe gas motions in a weak bar potential. This model solves the equation of motion which includes a damping-force term to emulate the collisional nature of gas, and obtains closed orbits of gas in bar. This model has been applied to a galaxy NGC 5005 (Sakamoto, Barker & Scoville 2000), and similar models have been successfully used to infer the presence of bars in edge-on galaxies which show characteristic patterns on PV diagrams (Binney et al. 1991; Achtermann & Lacy 1995; García-Burillo & Guélin 1995; Kuijken & Merrifield 1995).

Figure 12 displays our model of gas orbits in a bar potential that reproduces main features in the zeroth-, first-moment maps, and PV diagram of NGC 3079. We here took the same potential model as Sakamoto, Barker & Scoville (2000) by

$$\Phi(r,\theta) = (1-\epsilon\cos 2\theta)\frac{v_0^2}{2}\log(1+(r/a)^2), \qquad (3)$$

where the first and second terms stand for disk and bar potentials respectively. For this particular case we adopted the characteristic radius $a = 6''$ (456 pc), rotation velocity $v_0 = 240\,\mathrm{km\,s^{-1}}$ and bar strength $\epsilon = 0.04$ to match the observations. We chose the pattern speed of $\Omega_\mathrm{b} = 55\,\mathrm{km\,s^{-1}\,kpc^{-1}}$ based on consideration given in § 4.2. The inner and outer ILR and corotation occur at the radii of $7.7''$ (582 pc), $10.5''$ (798 pc) and $57.1''$ (4.34 kpc) respectively. We assumed that the position angle of the bar (dashed line) from the north is $\mathrm{P.A._{int}} = 135°$ intrinsic to the disk, and $\mathrm{P.A._{sky}} = 158°$ on the sky. On the galaxy disk, this position angle of the bar differs by 30° from that of the galaxy major axis which runs horizontally in Figure 12 (*top*).

EDITOR: PLACE FIGURE 12 HERE.

Our parameters of the bar chosen to match the CO observations are in good agreement with the values that Veilleux, Bland-Hawthorn & Cecil (1999) have derived by fitting an oval-orbit model to their Hα velocity field of NGC 3079 ($\Omega_\mathrm{b} \sim 60\,\mathrm{km\,s^{-1}\,kpc^{-1}}$; $\mathrm{P.A._{bar}} = 130 \pm 10°$; axes ratio of oval orbits 0.7). Beyond our particular choices of the parameters, the features of gaseous closed orbits described below are general (Wada 1994; Lindblad & Lindblad 1994), and have been established in numerical simulations (Wada 1994; Koda & Wada 2002).

Closed orbits in bar have elongation in general; the position angle of the elongation ψ is measured clockwise from the bar major axis (dashed line in Figure 12 *top*), in the rest of discussion. For collisionless star-like particles, two families of closed orbits are dominant: x_1-orbits have elongation with $\psi = 0°$ and dominate outside of the outer ILR and inside of the inner ILR, while x_2-orbits elongate with $\psi = 90°$ and are dominant between the ILRs. Orbits for gaseous particles show similar families at the same loci (Figure 12 *top*), while gaseous x_1-orbits have elongation toward the leading edge of the bar ($\psi > 0°$) owing to the damping force, and gaseous x_2-orbits elongate opposite ($\psi < 90°$).

4.2. *The Origin of The Main Disk and Spiral Arms*

The main disk and spiral arms may originate from gaseous x_1-orbits. The position angle ψ of orbits changes with radius owing to the damping force, producing crowded regions of the orbits (Figure 12). The crowdings of the gaseous x_1-orbits which appear at the leading edge of the bar result in the spiral arms (or so-called offset ridges), which are similar to those on the molecular disk of NGC 3079. The slight enhances of CO emission in the zeroth-moment map of NGC 3079 (Figure 2) may arise from the high gas densities at the crowded regions. The streamlines belonging to the x_1-orbits extend entirely to the disk, producing the main disk.

Our model streamlines have sharp turns at the spiral arms. Such features, accompanied with shocks, have been observed by other authors (Athanassoula 1992; Athanassoula & Bureau 1999) in full hydrodynamical simulations. These turns can produce double-peak features in line-profiles observed along the spiral arms (Figure 9), and agree spatially with the S-shaped twists on the first-moment map of NGC 3079 (Figure 2). Figure 13 shows a comparison between the observed and model PV diagrams; contours are from the observed one, while the symbols show the model one, where different symbols are used for gaseous particles on the spiral arms (squares) and on the main disk (dots). On this diagram again, the main disk and spiral arms of NGC 3079 well agree with the gaseous x_1-orbits and their crowdings respectively. These successful matches of the observations with the model lead us to a strong conclusion that the main disk and spiral arms are the consequences of gaseous x_1-orbits.

EDITOR: PLACE FIGURE 13 HERE.

In the context of our model, gas streamlines at the downstream side of the sharp turns are nearly perpendicular to our line-of-sight. Thus the line-of-sight velocity of the gas indicate the pattern speed of the bar. We estimate the pattern speed from the gradient of the spiral arms on the observed PV diagram, which appears to be

$\Omega_b = 55 \pm 10\,\mathrm{km\,s^{-1}\,kpc^{-1}}$; this is our adopted value to describe gas orbits, and consistent with the result by other authors ($60\,\mathrm{km\,s^{-1}\,kpc^{-1}}$ from Veilleux, Bland-Hawthorn & Cecil 1999, where the coincidence of corotation and bar-end was assumed).

4.3. *The Origin of The Nuclear Disk*

The nuclear disk may result from gaseous x_2-orbits. In Figure 13, the model PV diagram shows that the gaseous x_2-orbits (crosses) are in good agreement with the nuclear disk of NGC 3079. Figure 14 displays PV diagrams along the galaxy major axis for the orbits within the outer ILR. The three panels show PV cuts with $10''$-width (intrinsic to the galaxy) and positional offsets for the east, central and west sides of the model galaxy respectively. These panels reveal that the bends and twist of the ridges discussed in §3.3 (see Figure 10) are also reproduced in our model: the top and bottom panels show bends downward and upward respectively, while the middle panel shows a twist upward (at the left-hand side) and downward (right-hand). Since purely rotating disk cannot produce this type of symmetric bends and twist, the gas on the nuclear disk must take oval orbits. Our gaseous x_2-orbits naturally reproduce the observed properties of the nuclear disk.

EDITOR: PLACE FIGURE 14 HERE.

For later discussion in § 4.4, we discuss the position angle of the x_2-orbits on the nuclear disk here in advance. The major axis of the orbits are inclined clockwise to the south from our line-of-sight in our current configuration (Figure 11). On the other hand, orbits inclined in the opposite can also reproduce the nuclear disk on the PV diagram (Figure 4). These orbits however make the ridges on the eastern and western PV diagrams (Figure 14) bend in the opposite directions, thus cannot match the observations (Figure 10). Therefore the orbits on the nuclear disk must have inclination southward from our line-of-sight, like our gaseous x_2-orbits.

Many barred galaxies show intense concentration of CO emission in their central parts (Sakamoto et al. 1999b; Sakamoto, Barker & Scoville 2000). NGC 3079 also have such concentration in the nuclear disk region (see Figure 8). This feature is well explained in the scenario for gas motions in bar: gas flow on x_1-orbits like ours leads to offset shocks at the leading edge of a bar, and results in an inflow of gas toward the nuclear region. Then the inflowing gas on the x_1-orbits collides with gaseous x_2-orbits near the pericenter of the x_1-orbits, entering onto the gaseous x_2-orbits, thus increasing mass densities in the nuclear disk. This scenario has been confirmed in hydrodynamical simulations (Piner, Stone & Teuben 1995; Athanassoula & Bureau 1999). The closed-orbit model does not predict such orbit transitions of the gas, however, our model with gaseous x_1- and x_2-orbits is quite suggestive of this scenario, and possibly produce the intense CO concentration within the nuclear disk of NGC 3079.

4.4. *The Origin of The Nuclear Core*

Our current model is successful in understanding the main features on the molecular disk of NGC 3079, which are the consequences of gas motions under a weak bar. However the model does not explain the nuclear core which appears in the PV diagram as high velocity-peaks near the galaxy center (Figure 4). Owing to our ability to match the observations with our model for a bar, it is natural to attribute the high velocities to another origin, a massive central component, besides bar. There however is a little possibility that the high velocities may arise from gaseous x_1-orbits within the inner ILR which could elongate along our line-of-sight. However the gaseous x_1-orbits are not the likely origin for two reasons.

(1) Our gaseous x_1-orbits within the inner ILR ($7.7''$) look near circular, thus cannot show high velocities at their pericenter. Numerical experiments have also shown similar features: circular orbits at innermost regions (Piner, Stone & Teuben 1995; Athanassoula & Bureau 1999). In the intensive study of PV diagrams in bar by Bureau & Athanassoula (1999) and Athanassoula & Bureau (1999), the x_1-orbits within the inner ILR do not produce any significant features (and velocity-peaks) on PV diagrams. These all imply no significant contribution of the x_1-orbits within the inner ILR to our PV diagram. (2) Even if the gaseous x_1-orbits are elongated, they must be near perpendicular to our line-of-sight, and cannot show us high velocities which occur at their pericenter for the following reason. The position angles ψ of x_1- and x_2-orbits, measured clockwise from the bar to the north (Figure 12 *top*), are intrinsically $\psi_{x_1} = 0°$ and $\psi_{x_2} = 90°$ respectively for collisionless stars. Owing to the damping force (working as viscosity), the two orbits drag each other and make $\psi_{x_1} > 0°$ and $\psi_{x_2} < 90°$ for collisional gas. This mechanism does not allow ψ_{x_1} to become larger than ψ_{x_2}. In addition to $\psi_{x_1} < \psi_{x_2}$, our gaseous x_2-orbits (nuclear disk) of NGC 3079 have to be inclined southward from our line-of-sight for the reason discussed in § 4.3. Thus the elongated gaseous x_1-orbits (if exist) must be near perpendicular to our line-of-sight, and cannot show the observed high-velocity features.

Central components with high velocities are often found in rotation-curve studies of external galaxies (Sofue et al. 1999). Their origin has been uncertain because detailed kinematics and effect of bar on gas disks could not be clarified. Therefore this is the first obvious evidence that there exists a massive component at the galaxy center.

5. CENTRAL ROTATION CURVE AND MASSIVE CORE

We discussed in §4.4 that the high velocity peaks at the radius of $\sim 1''$ in the PV diagram are not likely to result from noncircular motions driven by a bar, but is a consequence of circular rotation around the nuclear core. Thus we can estimate the central dynamical mass using a rotation curve.

5.1. *Central Rotation Curve*

Observed PV diagram in galaxy center suffers from large intrinsic velocity dispersions, and spill-in of emission from outer low velocity components owing to finite spatial resolution and slit width. Thus central rotation curve is not straightforwardly obtained from an observed PV diagram. We adopt the Takamiya & Sofue method (TS method; Takamiya & Sofue in private communication, and see Sofue & Rubin 2001) to obtain rotation curve of the nuclear core. This method is designed to iteratively determine a

rotation curve in an innermost region of a galaxy so that a model PV diagram calculated from the rotation curve and galaxy's emission profile could reproduce the original diagram.

Figure 15 displays PV diagrams and rotation curves of the nuclear core: the left-hand panel shows the observed one along the galaxy major axis with $1''$ slit-width, while the middle and right-hand panels show the calculated ones in the TS method and in the peak-tracing method respectively. The emission profile at the center ($\sim 1''$) cannot be derived directly from our data owing to our spatial resolution ($\sim 2''$). But the observations are indicative of its very sharp gradient, because even a point source can reproduce our observed profile through a convolution with our synthesized beam. Thus we assumed the emission profile as an analytic function of an exponential with the scale length of $1''$, which well reproduces observed features of the PV diagram. We assumed intrinsic velocity dispersions of $60\,\mathrm{km\,s^{-1}}$ (e.g. $15-50\,\mathrm{km\,s^{-1}}$ in the Galactic center from Bally, Stark & Wilson 1988, which is less active than NGC 3079).

EDITOR: PLACE FIGURE 15 HERE.

The PV diagram and rotation curve from the TS method show that the envelope of the observed PV diagram requests a sharp rise of the rotation curve at the central region. The observed emission at around $0\,\mathrm{km\,s^{-1}}$, which is not well reproduced in the TS method, may be contaminated by the emission from the nuclear disk surrounding the nuclear core. For a comparison, the right-hand panel displays the PV diagram using the rotation curve derived by tracing peak-intensity velocities of the observed PV diagram (the peak-tracing method); this method is often used to obtain rotation curves, but fails in reproducing the observed high velocity at the central part.

5.2. *Mass Estimation and Central Massive Core*

The dynamical mass within a radius r is estimated by

$$M_{\rm dyn} = 2.3\times10^5 \left(\frac{r}{\rm kpc}\right)\left(\frac{v(r)}{\rm km\,s^{-1}}\right)^2 M_\odot. \qquad (4)$$

Our spatial resolution is about $2''$ (152 pc), and the rotation velocity at this radius is $220\,\mathrm{km\,s^{-1}}$ from the rotation curve in the TS method (Figure 15 *middle*). Thus the dynamical mass within the central 152 pc of NGC 3079 is estimated to be $M_{\rm dyn} = 1.7\times10^9 M_\odot$. The ratio of dynamical mass to the total molecular gas mass ($3.0\times10^8 M_\odot$ from §3.4) in the nuclear core is $M_{\rm gas}/M_{\rm dyn} = 18\%$.

Beyond our spatial resolution ($\sim 2''$), the rotation curve is meaningful at the radius less than $2''$: Our spatial resolution of $\sim 2''$ means that we can distinguish two emission peaks with a spatial separation larger than $2''$ on a single channel map or zeroth-moment map. However on the PV diagram and rotation curve, the additional parameter, velocity, would provide a finer spatial resolution, because two emission peaks with different velocities can be resolved *spatially* even if their separation is less than $2''$. Then the spatial resolution will be determined by the typical error of a gaussian fit to a point source, which depends on the signal-to-noise ratio, and in our case $\ll 1''$ (see Condon 1997). Therefore the velocity of $200\,\mathrm{km\,s^{-1}}$ at the radius of $1''$ (76 pc) is meaningful, and implies the dynamical mass of $M_{\rm dyn} = 7.0\times10^8 M_\odot$ within the radius of 76 pc. The derived masses are listed in Table 4.

Recently central supermassive black holes with mass $10^{7-8} M_\odot$ have been found in many AGNs (Miyoshi et al. 1995; Wandel, Peterson & Malkan 1999; Ishihara et al. 2001). In the case of NGC 3079, VLBI observations of H_2O maser emission indicate that its central mass within 0.5 pc is $\sim 10^6 M_\odot$ (Trotter et al. 1998). Our mass $\sim 10^9 M_\odot$ within ~ 100 pc cannot be attributed to the central supermassive black hole.

6. CONCLUSIONS

We have made CO(1-0) observations of Hα/Radio lobe galaxy NGC 3079 with the Nobeyama Millimeter Array, and reported characteristic features and gas dynamics on the molecular disk in the central 4.5 kpc ($1'$).

1. Our observations show four distinct components in the molecular disk: the main disk, spiral arms, nuclear disk, and nuclear core.

2. The main disk extends along the galaxy major axis. We detected the inner region of this component, within the radius of ~ 2 kpc on a zeroth-moment map, while its full extent is not covered in our synthesis observations. Molecular gas shows smooth distribution on the main disk, and has gas mass of $5\times10^9 M_\odot$ within central ~ 2 kpc.

3. The spiral arms are superimposed on the main disk, and extend entirely to the main disk. They form a Z-shaped pattern on the sky. Abrupt velocity change of up to $\sim 200\,\mathrm{km\,s^{-1}}$ is observed along the spiral arms, in S-shaped twists of isovelocity contours and double velocity-peak features on spectra. This component and the nuclear disk forms the so-called "figure-of-eight" pattern on a PV diagram, which sometimes appears in edge-on barred galaxies.

4. The nuclear disk has an extent of ~ 600 pc radius, appearing in PV diagrams. Molecular gas shows intense concentration on the nuclear disk, where gas surface density is an order of magnitude higher than the typical of nearby galaxies. Its appearances (bends and twist) on PV diagrams are indicative of oval motions of the gas on it, rather than circular. And the position angle of the oval orbits are inclined southward from our line-of-sight.

5. The nuclear core has a radius smaller than ~ 150 pc, which is unresolved in our current resolution. The gas mass within central ~ 150 pc amounts to $3\times10^8 M_\odot$. This component shows very high velocity $\sim 200\,\mathrm{km\,s^{-1}}$ at the radius of central ~ 100 pc on PV diagram.

6. A weak bar model successfully explain the features of the main disk, spiral arms, and nuclear disk in zeroth- and first-moment maps, PV diagrams, and spectrum of each spatial point. The main disk and spiral arms result from gaseous x_1-orbits and their crowdings respectively. The nuclear disk arises from gaseous x_2-orbits. The gas concentration on the nuclear disk is also explained in the context of our model: the gas on the x_1-orbits moves along spiral arms (or offset shocks), collide with the gas on x_2-orbits, and is accumulated onto the nuclear disk. Assuming that the gas on spiral arms moves along streamline perpendicular to our line-of-sight, the pattern speed of the bar can be estimated to be $55\pm10\,\mathrm{km\,s^{-1}\,kpc^{-1}}$.

7. Our successful model however does not explain the

high velocity of the nuclear core. Moreover, any orbit caused by a bar is not likely to produce that component. Thus we confidently attribute it to a central massive core with dynamical mass of $10^9 M_\odot$ within the central 100 pc. It is three orders of magnitude more massive than the mass of a central supermassive black hole. This is the first clear evidence for the presence of the central massive core, other than black hole.

We are grateful to NRO staffs and Rainbow team members for their help with observations. J. K. thanks Dr. Keiichi Wada and Toshihiro Handa for fruitful discussions and continuous encouragements, and Dr. Kentaro Aoki for his help with the analysis of the *HST* data. J. K. was financially supported by the Japan Society for the Promotion of Science for Young Scientists.

REFERENCES

Achtermann, J. M. and Lacy, J. H. 1995, ApJ, 439, 163
Arimoto, N., Sofue, Y., and T. Tsujimoto 1996, PASJ, 48, 275
Athanassoula, E. 1992, MNRAS, 259, 345
Athanassoula, E. and Bureau, M. 1999, ApJ, 522, 699
Bally, J., Stark, A. A., and Wilson, R. W. 1988, ApJ, 324, 223
Bureau, M. and Athanassoula, E. 1999, ApJ, 522, 686
Brandt, J. C. 1965, MNRAS, 129, 309
Combes, F., Debbasch, F., Friedli, D., and Pfenniger, D. 1990, A&A, 233, 82
Cox A. N. 2000, Allen's astrophysical quantities (4th ed), (New York: Springer-Verlag)
Bally, J., Stark, A. A., Wilson, R. W. and Hekel, C. 1988, ApJ, 324, 223
Binney, J. Gerhard, O. E., Stark, A. A., Bally, J., and Uchida, K. I., 1991, MNRAS, 252, 210
Braine, J. et al. 1993, A&AS, 97, 887
Cecil, G., Bland-Hawthorn, J., Veilleux, S. and Filippeko, A. V. 2001, ApJ, 555, 338
Clemens, D. P., Sanders, D. B., and Scoville, N. Z. 1988, ApJ, 327, 139
Condon, J. J. 1997, PASP, 109, 166
Dame, T. M., Hartmann, D., and Thaddeus, P. 2001, ApJ, 547, 792
de Vaucouleurs, G., de Vaucouleurs, A., Corwin, H. G., Buta, R. J., Paturel, G., and Fouque, P. 1991, Third Reference Catalog of Bright Galaxies (New York: Springer-Verlag)
Duric, N. and Seaquist, E. R. 1988, ApJ, 326, 574
Fabbiano, G., Kim, D. -W., and Trinchieri, G. 1992, ApJS, 80, 531
Filippenko, A. V. and Sargent, W. L. W. 1992, AJ, 103, 1
Ford, H. C., Dahari, O., Jacoby, G. H., Crane, P. C., and Ciardullo, R. 1986, ApJ, 311, 7
García-Burillo, S. and Guélin, M. 1995, A&A, 299, 657
Handa, T., Nakai, N, Sofue, Y., Hayashi, M. and Fujimoto, M. 1990, PASJ, 42, 1
Handa, T., Sofue, Y., Ikeuchi, S., Kawabe, R., and Ishizuki, S. 1992, PASJ, 44, L227
Hawarden, T. G., Israel, F. P., Geballe, T. R., and Wade, R. 1995, MNRAS, 276, 1197
Heckman, T. M. 1980, A&A, 87, 152
Heckman, T. M., Armus, L., and Miley, G. K. 1990, ApJS, 74, 833
Henkel, C, Güsten, R., Downes, D., Thum, C., Wilson, T. L., and Biermann 1984, A&A, 141, L1
Humason, M. L, Mayall, N. U., and Sandage, A. R. 1956, AJ, 61, 97
Irwin, J. A. and Seaquist, E. R. 1988, ApJ, 335, 658
Irwin, J. A. and Seaquist, E. R. 1991, ApJ, 371, 111
Irwin, J. A., Seaquist, E. R., Taylor, A. R., and Duric, N. 1987, ApJ, 313, 91
Irwin, J. A., and Sofue, Y. 1992, ApJ, 396, 75
Ishihara, Y., Nakai, N., Iyamoto, N., Makishima, K., Diamond, P., and Peter, H. 2001, PASJ, 53, 215
Koda, J. and Wada, K. 2002, submitted to ApJ
Kohno, K. et al. 2001, in ASP Conf. Proc. **, The Central kpc of Starbursts and AGN, ed. Knapen, J. H., Beckman, J. E., Shlosman, I., and Mahoney, T. J. (San Francisco: ASP), **
Kuijken, K. and Merrifield, M. R. 1995, ApJ, 443, 13
Merrifield, M. R. and Kuijken, K. 1999, A&A, 345, L47
Laine, S., Kenney, J. D. P., Yun, M. S., and Gottesman, S. T. 1999, ApJ, 511, 709
Lindblad, P. O. and Lindblad, P. A. B. 1994, in ASP Conf. Proc. 66, Physics of the Gaseous and Stellar Disks of the Galaxy, ed. King. I. R. (San Francisco: ASP), 29
Malhotra, S. 1994, ApJ, 433, 687
Mathewson, D. S., Ford, V. L., and Buchhorn, M. 1992, ApJS, 81, 413
Miyoshi, M., Moran, J., Henstein, J., Greenhill, L., Nakai, N., Diamond, P., and Inoue, M. 1995, Nature, 373, 127
Oka, T., Hasegawa, T., Hayashi, M., Handa, T., and Sakamoto, S. 1998, ApJ, 493, 730
Okumura, S. K., et al. 2000, PASJ, 52, 393
Pérez García, A. M., Rodríguez Espinosa, J. M., and Fuensalida, J. J. 2000, ApJ, 529, 875
Pietsch, W. Trinchieri, G., and Vogler, A. 1998, A&A, 340, 351
Piner, B. G., Stone, J. M., and Teuben, P. J. 1995, ApJ, 449, 508
Regan, M. W., Thornley, M. D., Helfer, T. T., Sheth, K., Wong, T., Vogel, S. N., and Bock, D. C. -J. 2001, ApJ, 561, 218
Regan, M. W., Sheth, K., and Vogel, S. N. 1999, ApJ, 526, 97
Rubin, V. C., Thonnard, N., and Ford, W. K. J. 1980, ApJ, 238, 471
Rubin, V. C., Thonnard, N., Ford, W. K. J., Burstein, D., 1982, ApJ, 261, 439
Rubin, V. C., Burstein, D., Ford, W. K. J., and Thonnard, N. 1985, ApJ, 289, 81
Sakamoto, K., Okumura, S. K., Ishizuki, S., and Scoville, N. Z. 1999a, ApJS, 124, 403
Sakamoto, K., Okumura, S. K., Ishizuki, S., and Scoville, N. Z. 1999b, ApJ, 525, 691
Sakamoto, K., Baker, A. J., and Scoville, N. Z. 2000, ApJ, 533, 149
Sandage, A., and Tamman, G. 1981, A Revised-Sharpley-Ames Catalog of Bright Galaxies (Washington, DC: Carnegie Institution of Washington)
Sawada-Satoh, S., Inoue, M, Shibata, K. M., Kameno, S., and Migenes, V. 2000, PASJ, 52, 428
Sofue, Y. 1995, PASJ, 47, 527
Sofue, Y. 1996, ApJ, 458, 120
Sofue, Y., and Irwin, J. A. 1992, PASJ, 44, 353
Sofue, Y. and Rubin, V. 2001, ARA&A, 39, 137
Sofue, Y., Tutui, Y., Honma, M., Tomita, A., Takamiya, T., Koda, J., and Takeda, Y. 1999, ApJ, 523, 136
Sofue, Y., Koda, J., Kohno, K., Okumura, S. K., Honma, M., Kawamura, A., and Irwin, J. A. 2001, ApJ, 547, 115
Soifer, B. T., Boehmer, L., Neugebauer, G., and Sanders, D. B. 1989 AJ, 98, 766
Sosa-Brito, R. M., Tacconi-Garman, L. E., and Lehnert, M. D. 2001, ApJS, 136, 61
Shaw, M., Wilkinson, A., and Carter, D. 1993, A&A, 268, 511
Trotter, A. S., Greenhill, L. J., Moran, J. M., Reid, M. J., Irwin, J. A., and Lo, K. Y. 1998, ApJ, 495, 740
Veilleux, S., Cecil, G., Bland-Hawthorn, J., Tully, R. B. 1994, ApJ, 433, 48
Veilleux, S., Bland-Hawthorn, J., and Cecil, G. 1999, ApJ, 118, 2108
Wada, K. 1994, PASJ, 46, 165
Wandel, A., Peterson, B. M., and Malkan, M. A. 1999, ApJ, 526, 579
Young, J. S., Claussen, M. J., and Scoville, N. Z. 1988, ApJ, 324, 115
Young, J. S., et al. 1995, ApJS, 98, 219
Zacharias, N., et al. 2000, AJ, 120, 2131

TABLE 1
PROPERTIES OF NGC 3079

Parameter	Value	Reference
Morphology	SB(s)c sp	1
	Sc pec:	2
Nuclear activity	LINER	3
	Type 2 Seyfert	4
Position of nucleus:		5
α(B1950)	9 58 35.02	
δ(B1950)	55 55 15.4	
$D_{25} \times d_{25}$	7.9×1.4	1
B_T(mag)	11.54	1
P.A. ($^\circ$)	165	1
Inclination ($^\circ$)	77	6
Distance (Mpc)	15.6	5
Linear scale (pc arcsec^{-1})	76	
$S_{60\mu m}$ (Jy)	50.17 $\pm$0.054	7
$S_{100\mu m}$ (Jy)	103.40 $\pm$0.154	7
$L_{\rm FIR}$ ($L_\odot$)[a].....	2.1×10^{10}	

[a] $L_{\rm FIR}$ was calculated as $3.75 \times 10^5 (D/\,{\rm Mpc})^2 (2.58 S_{60\mu m} + S_{100\mu m})$ in $Lsun$.

Note. — Reference.– (1) de Vaucouleurs et al. 1991; (2) Sandage & Tamman 1981; (3) Heckman 1980; (4) Ford et al. 1986; (5) Sofue & Irwin 1992; (6) Young et al. 1995; (7) Soifer et al. 1989

TABLE 2
PARAMETERS OF CO(1-0) CUBE

Parameter	Value
Configuration	AB+C+D
Weighting	NA
Field of view ($''$)	65
Synthesized beam:	
major axis ($''$)	1.9
minor axis ($''$)	1.6
P.A. ($^\circ$)	105
Velocity resolution (km s^{-1})	10.4
rms (mJy beam^{-1}).....	12

TABLE 3
KINEMATIC PARAMETERS OF THE NUCLEAR DISK

Parameter	Value
Dynamical center:	
α(B1950)	9 58 35.00
δ(B1950)	55 55 15.90
P.A (deg)	169
Inclination (deg)	79
$V_{\rm sys}$ (km s^{-1})	1147

Table 4
GAS AND DYNAMICAL MASSES

RADIUS[a]		$M_{\rm dyn}$	$M_{\rm gas}$[b]	$M_{\rm gas}/M_{\rm dyn}$
(arcsec)	(pc)	($10^9 M_\odot$)	($10^8 M_\odot$)	(%)
26	1976	22	46 (26)	21 (12)
2	152	1.7	3.0 (1.7)	18 (10)
1	76	0.7	–	–

[a]Radius in the galactic plane

[b]Gas mass is calculated with a conversion factor $X_{\rm CO} = 1.8 \times 10^{20} {\rm cm}^{-2} \, [{\rm K \, km \, s}^{-1}]^{-1}$ and the H abundance $X = 0.707$. The values in brackets are the ones with $X_{\rm CO} = 1.0 \times 10^{20} {\rm cm}^{-2} \, [{\rm K \, km \, s}^{-1}]^{-1}$ for high metaticity regions as galactic centers (Arimoto, Sofue and Tsujimoto 1996)

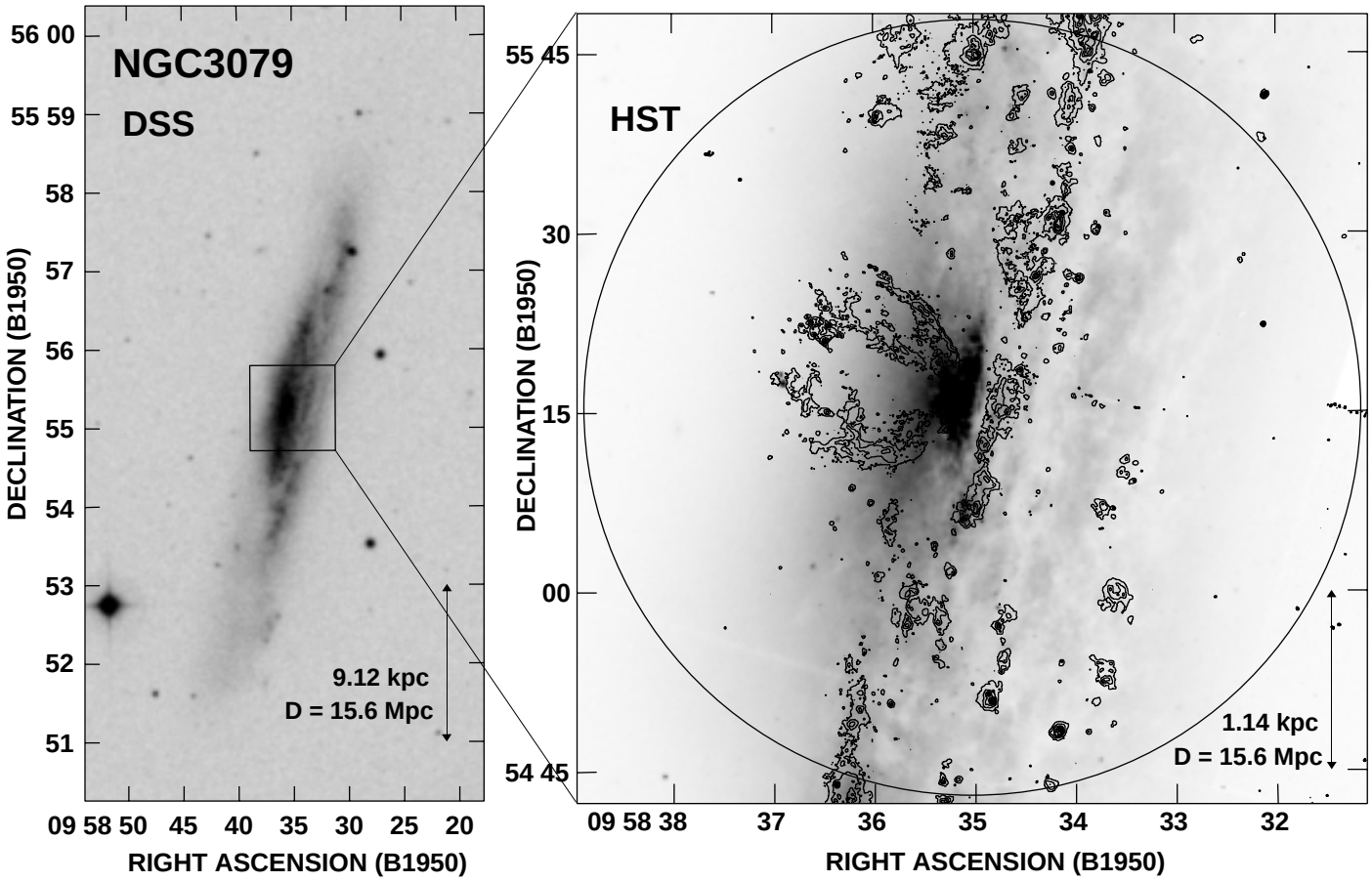

FIG. 1.— Optical images of NGC 3079. (a) R-band image from the Digitalized Sky Survey. (b) HST WFPC2 images of I-band (grey scale) and Hα + [N II] line emission (contour), obtained from the HST data archives (P.I. G. Cecil). Contours are at 2, 5, 15, 20, 30, 40, 50, 60, 70, 80, 90, 100% of the Hα + [N II] peak intensity. The circle represents the primary beam size of our CO(1-0) observations (65" HPBW). The absolute positions of both panels were calibrated using the USNO-A2.0 catalog (Zacharias et al. 2000), and uncertain to 0 $''$.5.

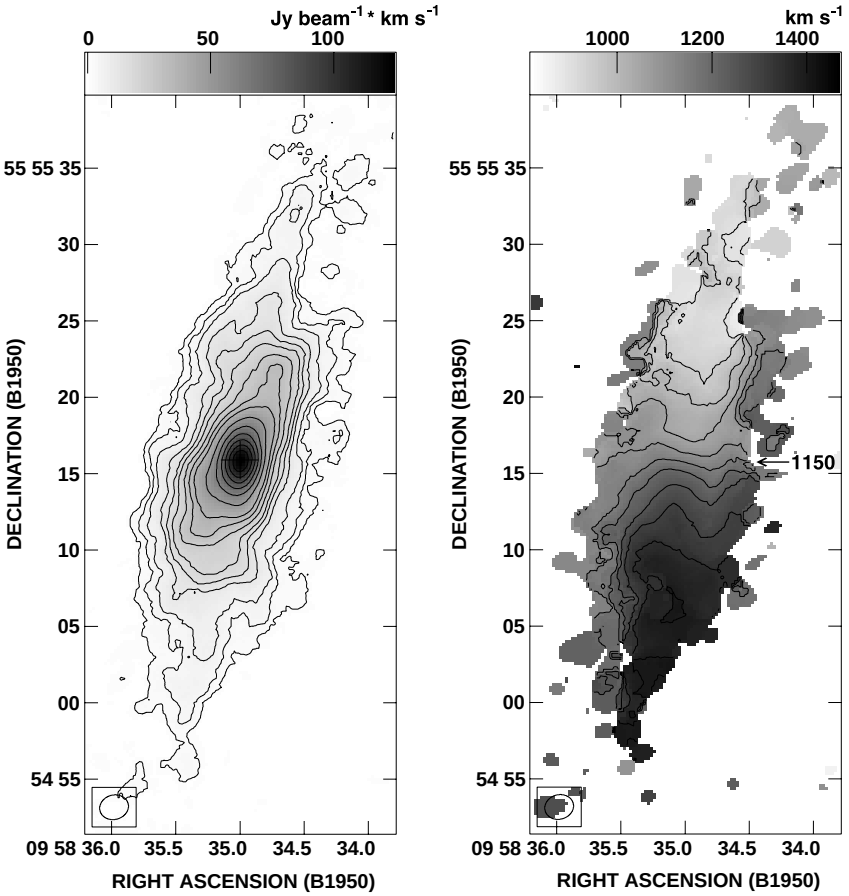

FIG. 2.— CO(1-0) zeroth- and first-moment maps in the central $20\,''\times48''$ ($1.52\,\mathrm{kpc}\times3.65\,\mathrm{kpc}$) region of NGC 3079. The synthesized beam ($1.9''\times1.6''$) is shown in the lower left corners. *Left:* The zeroth-moment map (integrated-intensity map). Contour levels are 1.5, 3, 5, 9, 12, 15, 20, 25, 30, 40, 50, 60, 70, 80, 90, 100 % of the peak integrated-intensity $1.25\times10^{\ 2}\,\mathrm{Jy\,beam^{-1}\ km\,s^{-1}}$. The clip level was set to 2.5σ where $1\sigma=12\,\mathrm{mJy\,beam^{-1}}$. The primary beam attenuation has not been corrected. *Right:* The first-moment map (intensity-weighted mean velocity map). Contours are drawn with an interval of $50\,\mathrm{km\,s^{\ -1}}$; The contour of $1150\,\mathrm{km\,s^{\ -1}}$ ($V_{\rm sys}=1147\,\mathrm{km\,s^{-1}}$) is pointed by an arrow. The clip level was set to 4σ to make this map.

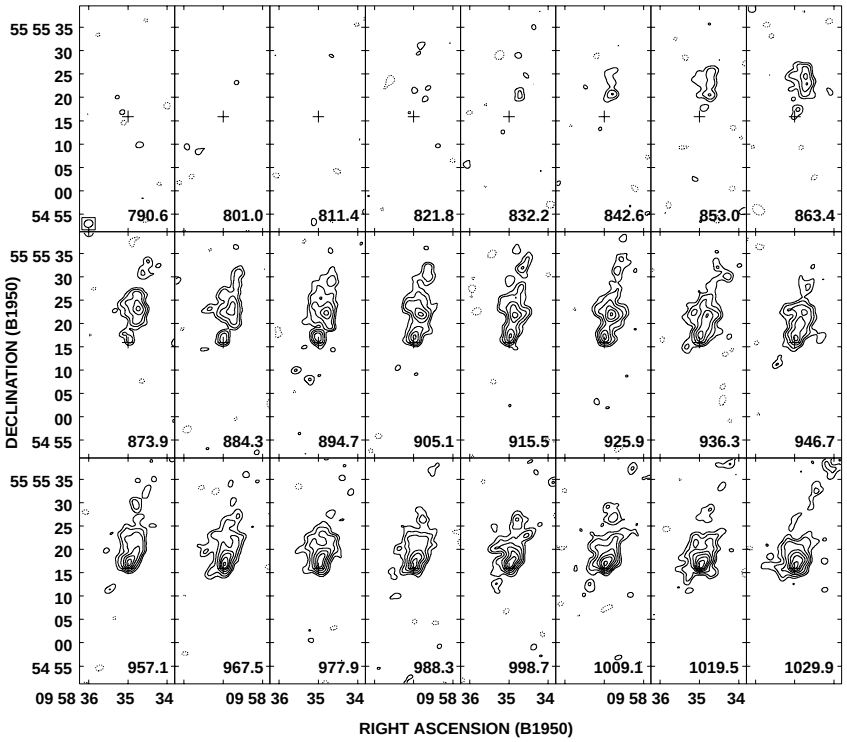

FIG. 3.— Channel maps in CO(1-0) emission. The channels have an interval of 10.4 km s $^{-1}$. Their central velocities ($V_{\rm LSR}$ in km s^{-1}) are labeled at the lower-right corners. Crosses show the position of the dynamical center (Table 3). Contour levels are -3, 3, 5, 8, 12, 16, 20, 25, 30σ, where $1\sigma = 12$ mJy beam^{-1}. Negative contours are dotted. No primary beam correction has been applied.

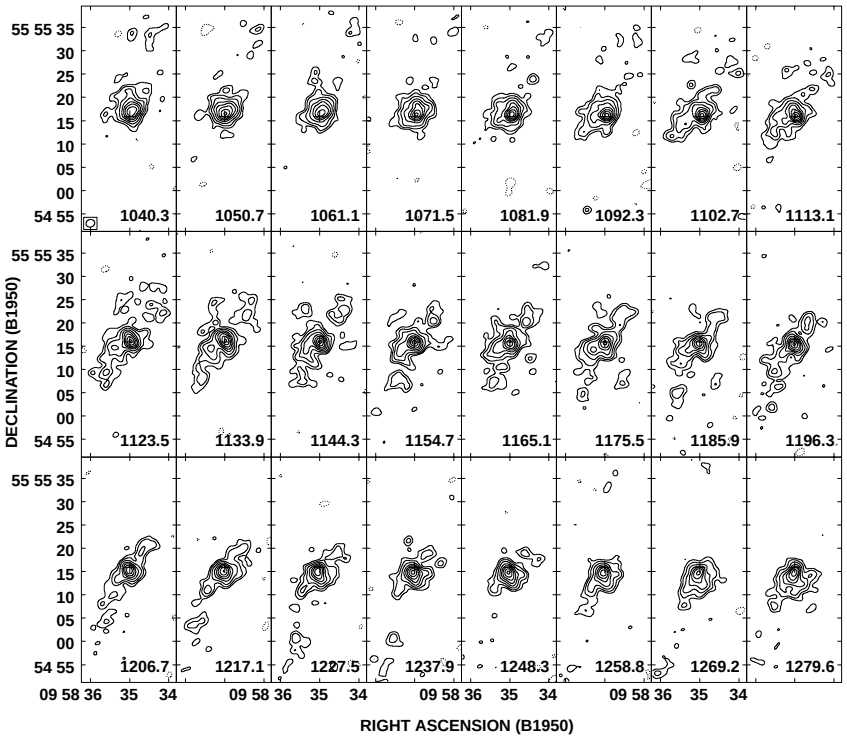

FIG. 3.— continued.

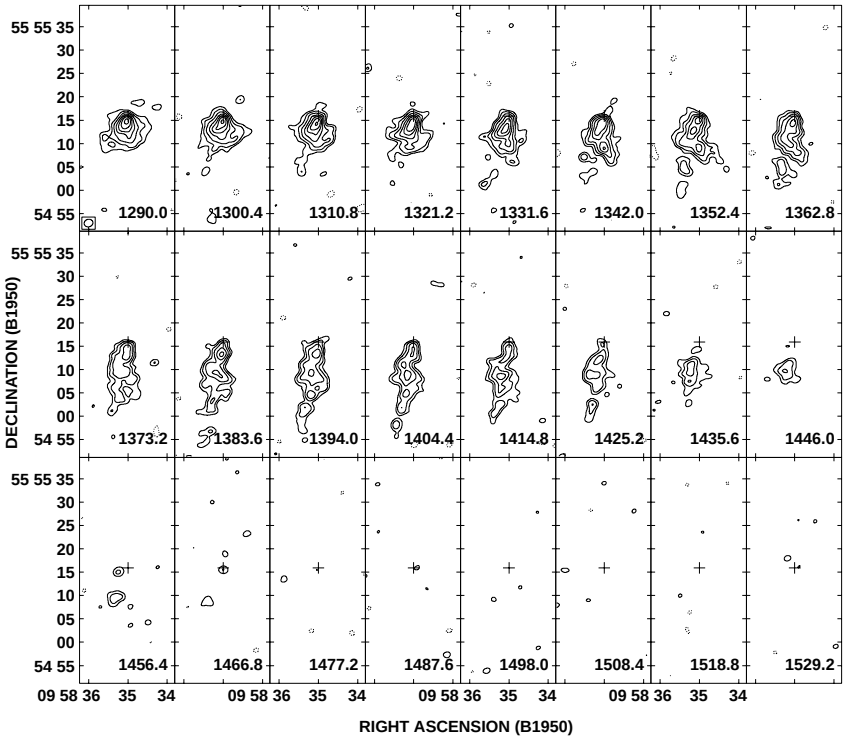

FIG. 3.— continued.

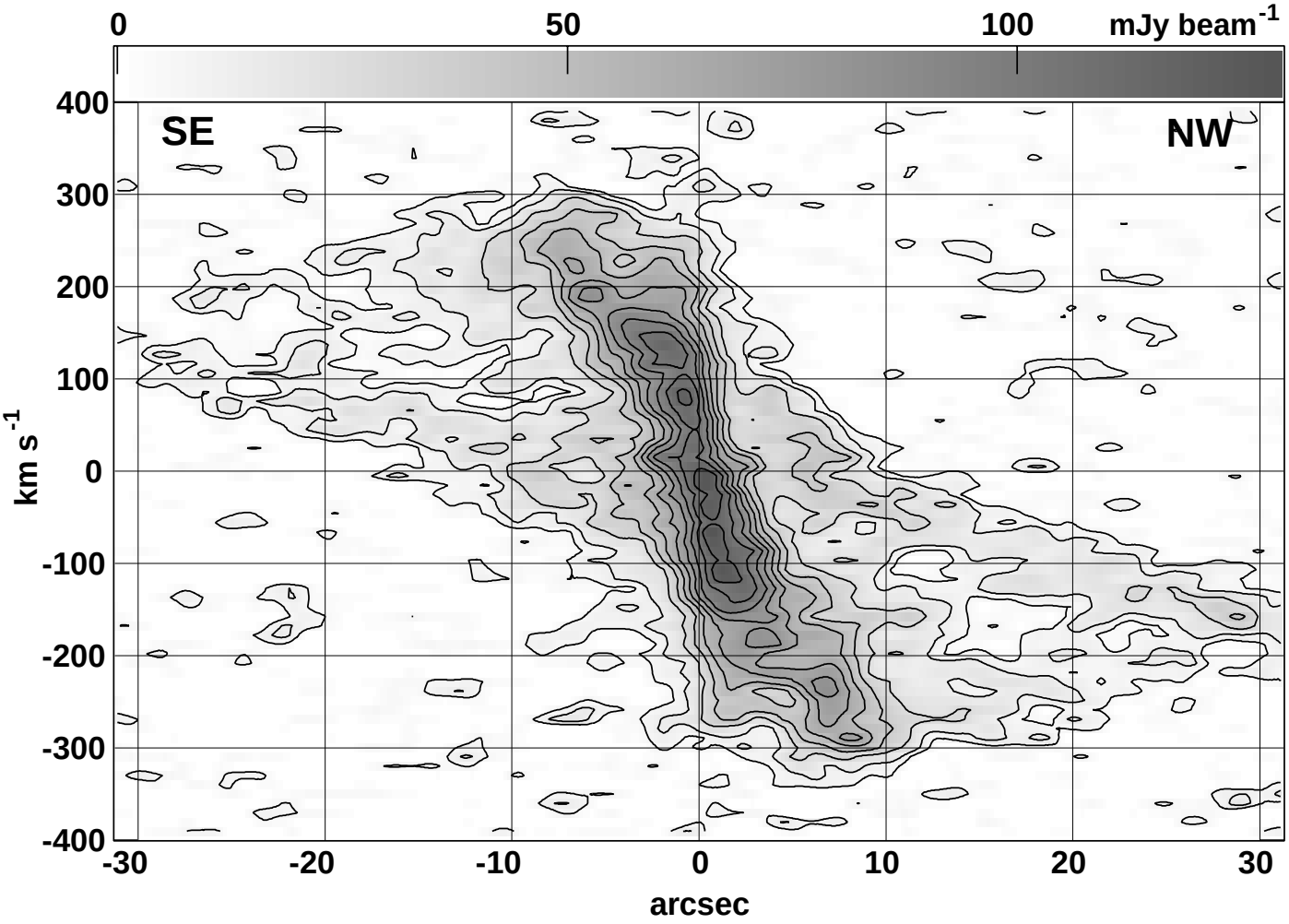

FIG. 4.— PV diagram of CO(1-0) emission along the major axis of NGC 3079 (P.A. = 165 °). The slit-width was set to be 12″, containing almost the entire emission in Figure 2. The axes are labeled relative to the dynamical center and systemic recession velocity (Table 3). Velocities have been corrected for inclination (77 °). Contours are at 5, 10, 20, 30, 40, 50, 60, 70, 80, 90, 100% of the peak intensity.

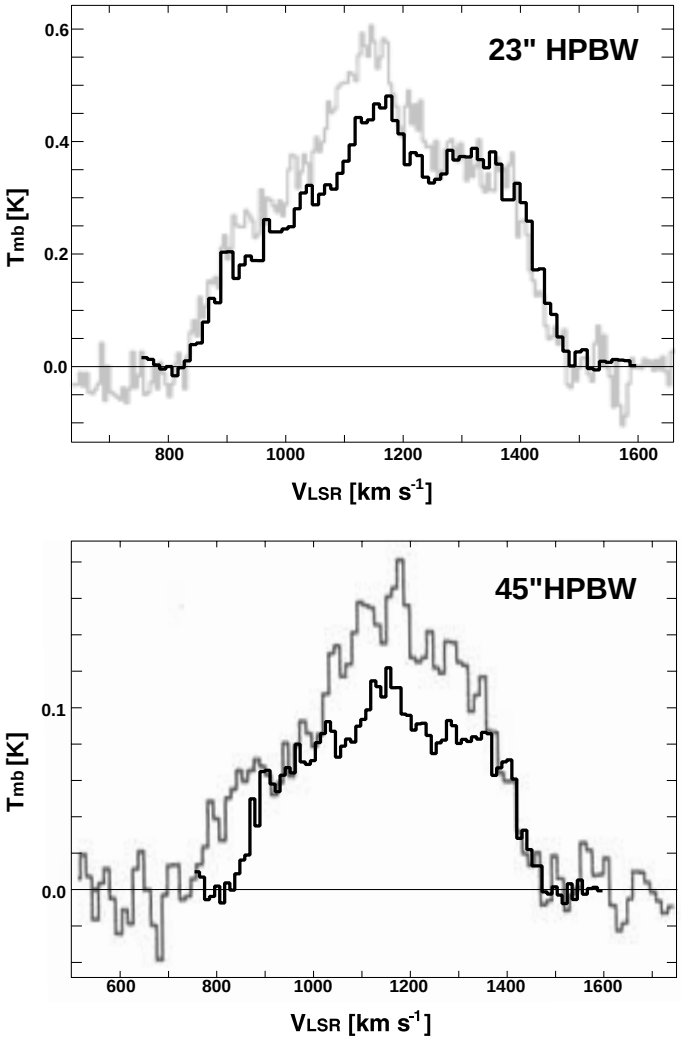

FIG. 5.— Comparisons of our CO(1-0) line spectra with the single-dish results of (a) IRAM 30 m from Braine et al. (1993) and (b) FCRAO 14 m telescopes from Young et al. (1995). The NMA cube was corrected for primary beam attenuation, convolved with single-dish beam sizes (23″ for IRAM and 45″ for FCRAO), and sampled at the pointing centers of the single-dish observations (α_{1950}, δ_{1950}) = ($09^{\rm h}58^{\rm m}35^{\rm s}.4$, $+55°55'11''.0$). Gray lines show the spectra from IRAM and FCRAO observations, whereas black lines show those from the NMA cube.

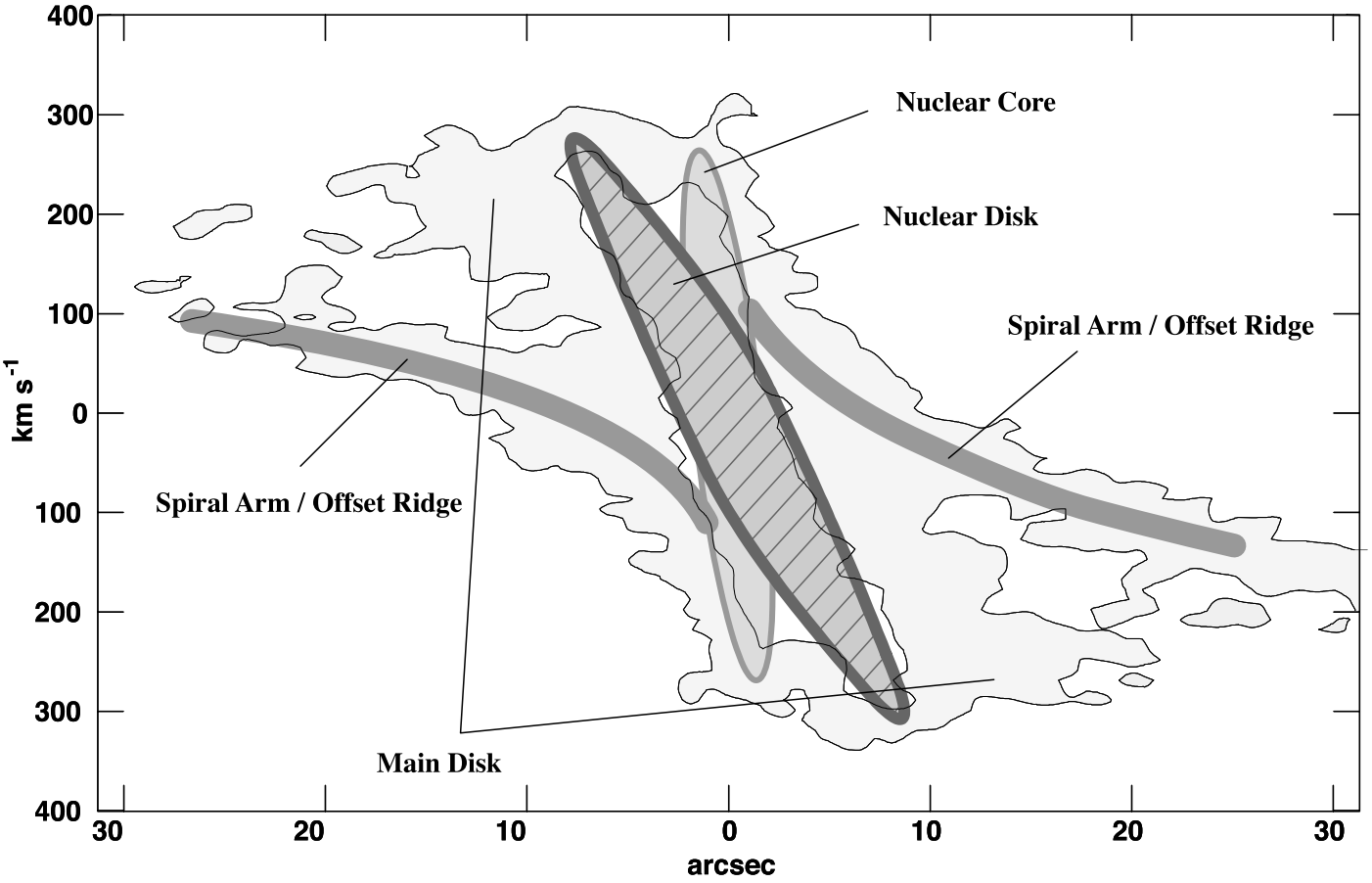

FIG. 6.— Schematic illustration of PV diagram. Four distinct components exist in the molecular disk of NGC 3079: main disk, spiral arms (or offset ridges), nuclear disk, and nuclear core.

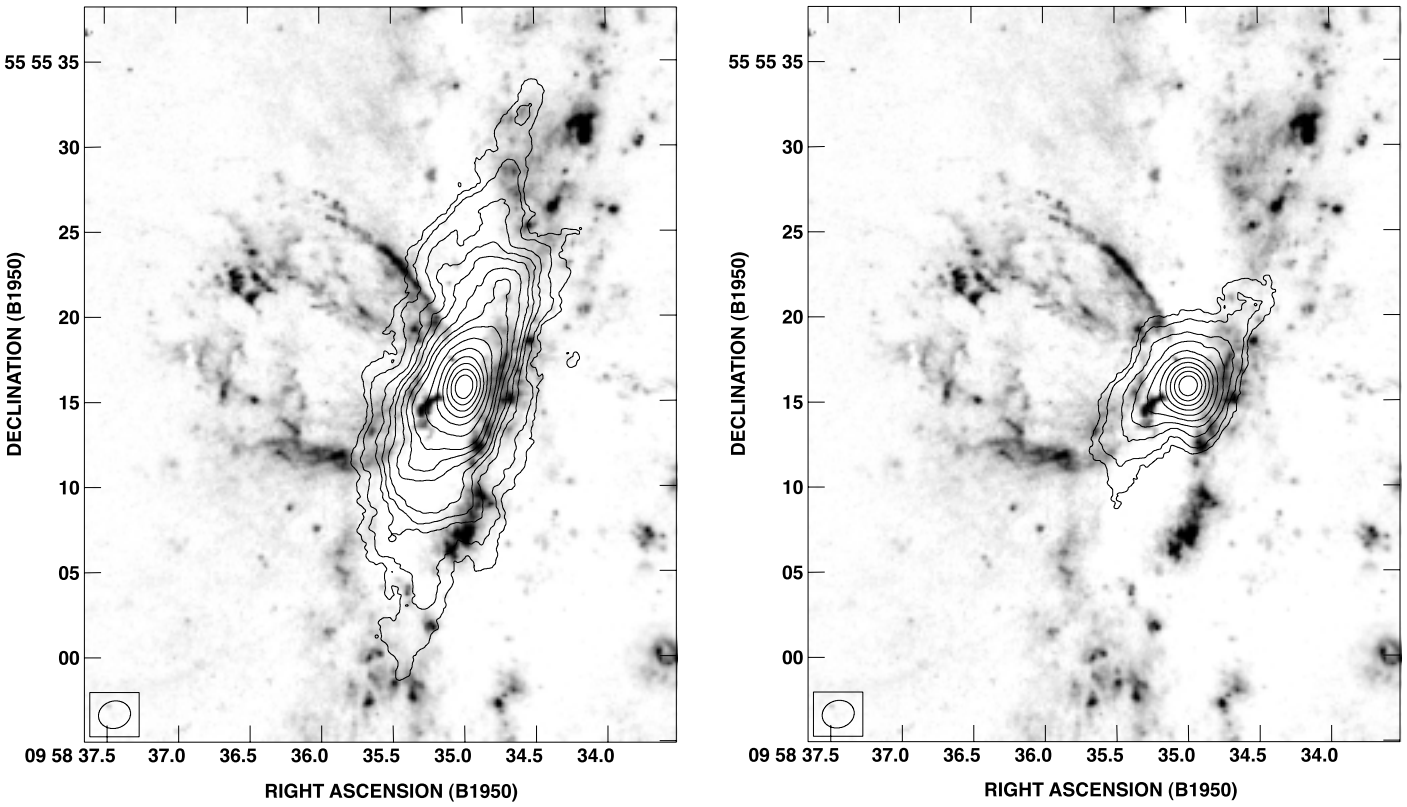

FIG. 7.— Comparisons of CO map (contours) with Hα + [N II] map (grayscale; from the HST archives). The absolute position of the HST image was calibrated with the USNO-A2.0 catalog, and accurate to about 0.5 $''$. The ellipses at the lower-left corners show the synthesized beam for the CO observations. The two panels show two sets of CO zeroth-moment maps, different in integrated velocity ranges. *Left:* CO map (contours) is derived by integrating the cube in the full velocity range where CO emission is detected. Contour levels are 3, 5, 9, 12, 15, 20, 25, 30, 40, 50, 60, 70, 80, 90, 100 % of the peak integrated intensity $1.25 \times 10^{\ 2}$ Jy beam^{-1} km s^{-1}. The molecular disk coincides with the void of HII regions at the center, and its center is coincident with the root of the Hα lobe. *Right:* CO map (contours) are derived by integrating the cube in the velocity range where the spiral arms are dominant in emission ($\Delta V = \pm 100$ km s$^{\ -1}$). Contour levels are 5, 10, 20, 30, 40, 50, 60, 70, 80, 90, 100 % of the peak integrated intensity 6.52×10 Jy beam$^{\ -1}$ km s^{-1}. The spiral arms extend from the root of the Hα lobe, and wind counterclockwise.

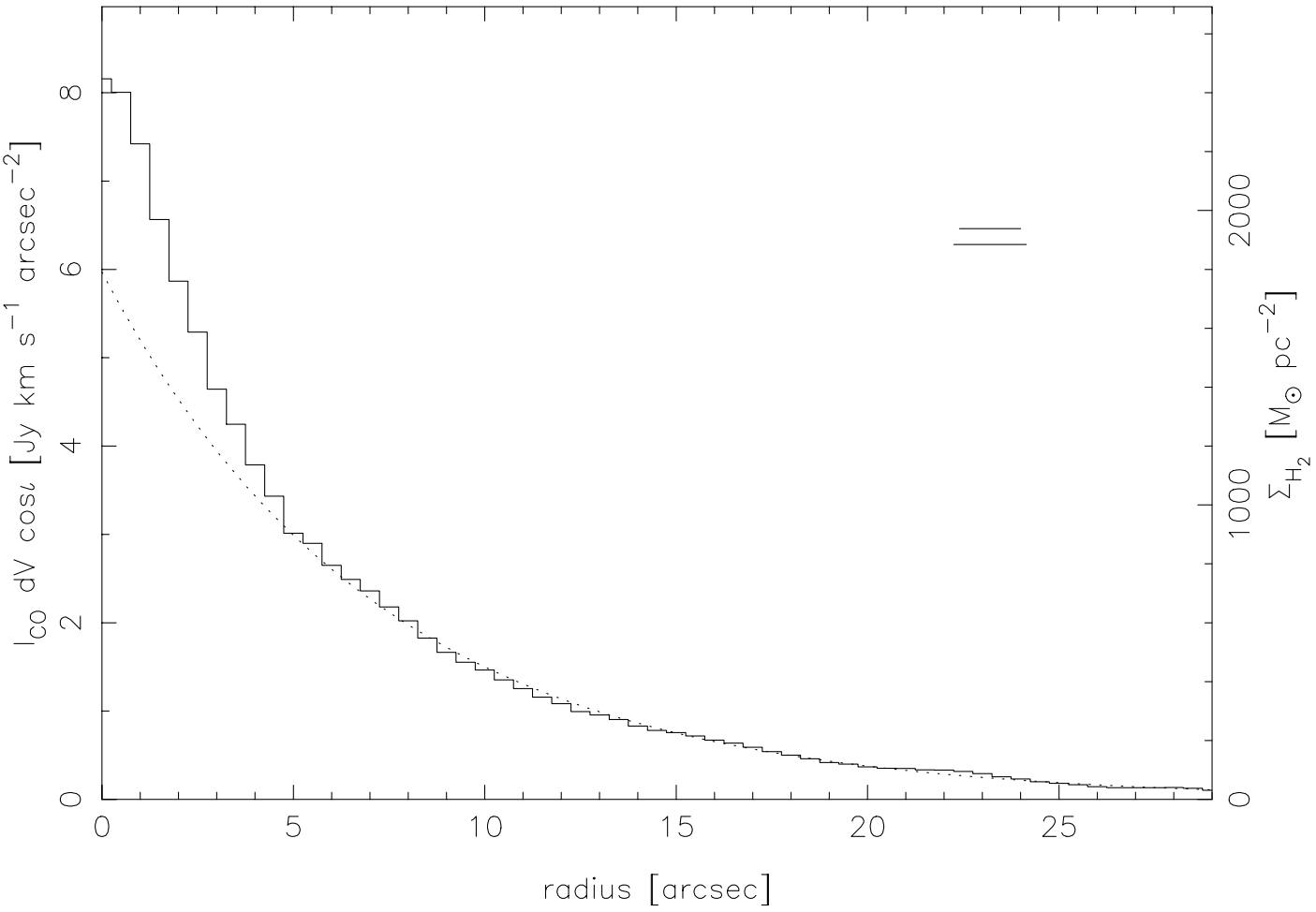

FIG. 8.— Radial distribution of CO emission. CO integrated intensities are azimuthally averaged with corrections for inclination and primary beam attenuation. No correction for missing flux (about $10-30\%$) has been applied. The surface densities on the right-hand axis are calculated by assuming the Galactic conversion factor $X_{\rm CO} = 1.8\times10^{20}{\rm cm}^{-2}\,[{\rm K\,km\,s}^{-1}]^{-1}$ (Dame, Hartmann and Thaddeus 2001). The two horizontal bars show the beam size along the major and minor axes ($1\,''.9 \times 1''.6$). Solid line presents the derived emission profile, while dotted line shows an fitted exponential profile, i.e. $5.97\exp(-r/7\,''.24)$, in the radii of $r > 5''$.

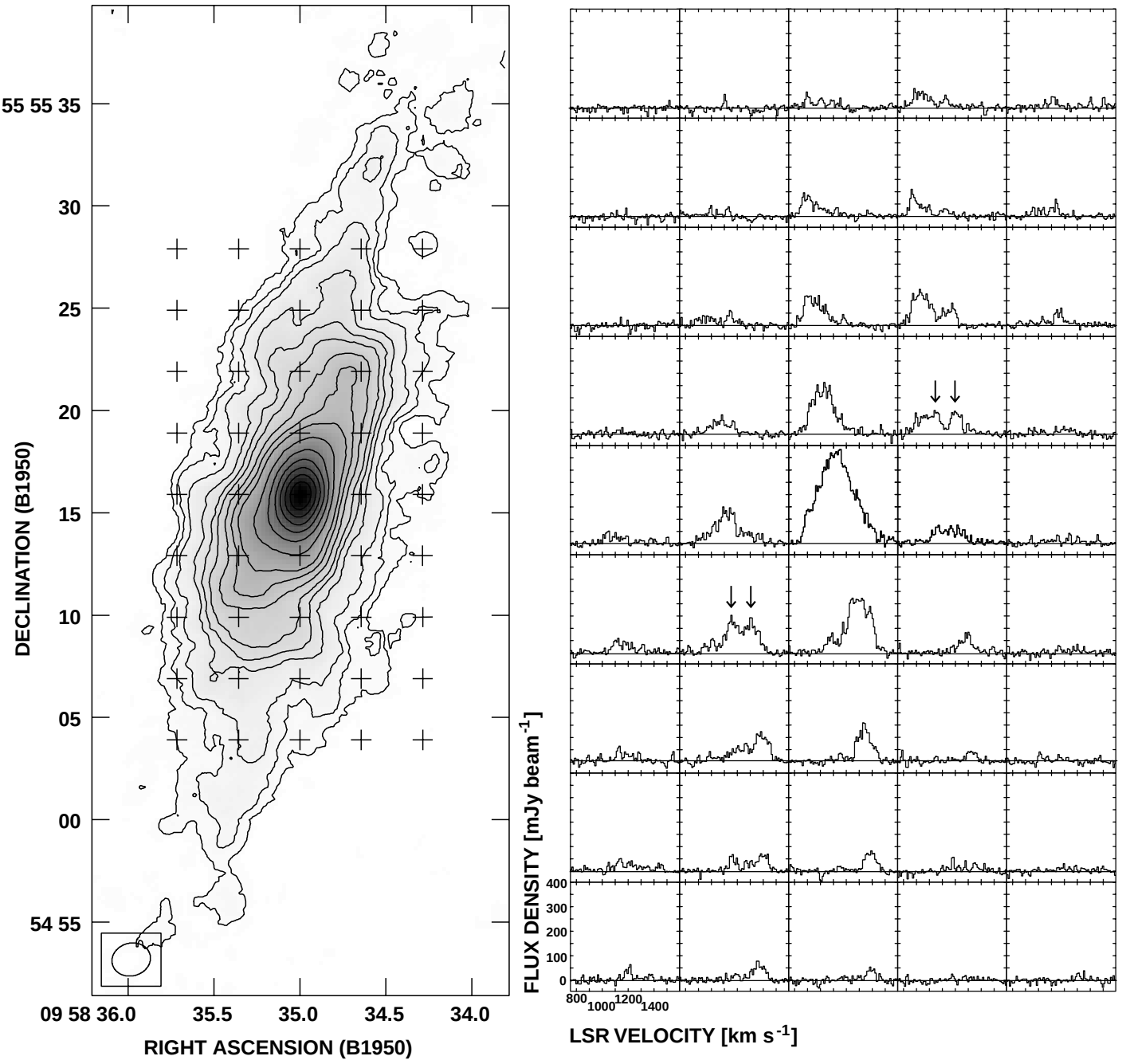

FIG. 9.— CO(1-0) line profiles and zeroth-moment map for reference. The line profiles are sampled at 5×7 points on the 3 ″-spacing grid (crosses on the left-hand panel), centered at the dynamical center (Table 3). Double-peak features in line profiles are observed along the spiral arms: arrows point two examples. The double-peaks are originated from distinct velocities between the main disk and spiral arms (or offset ridges).

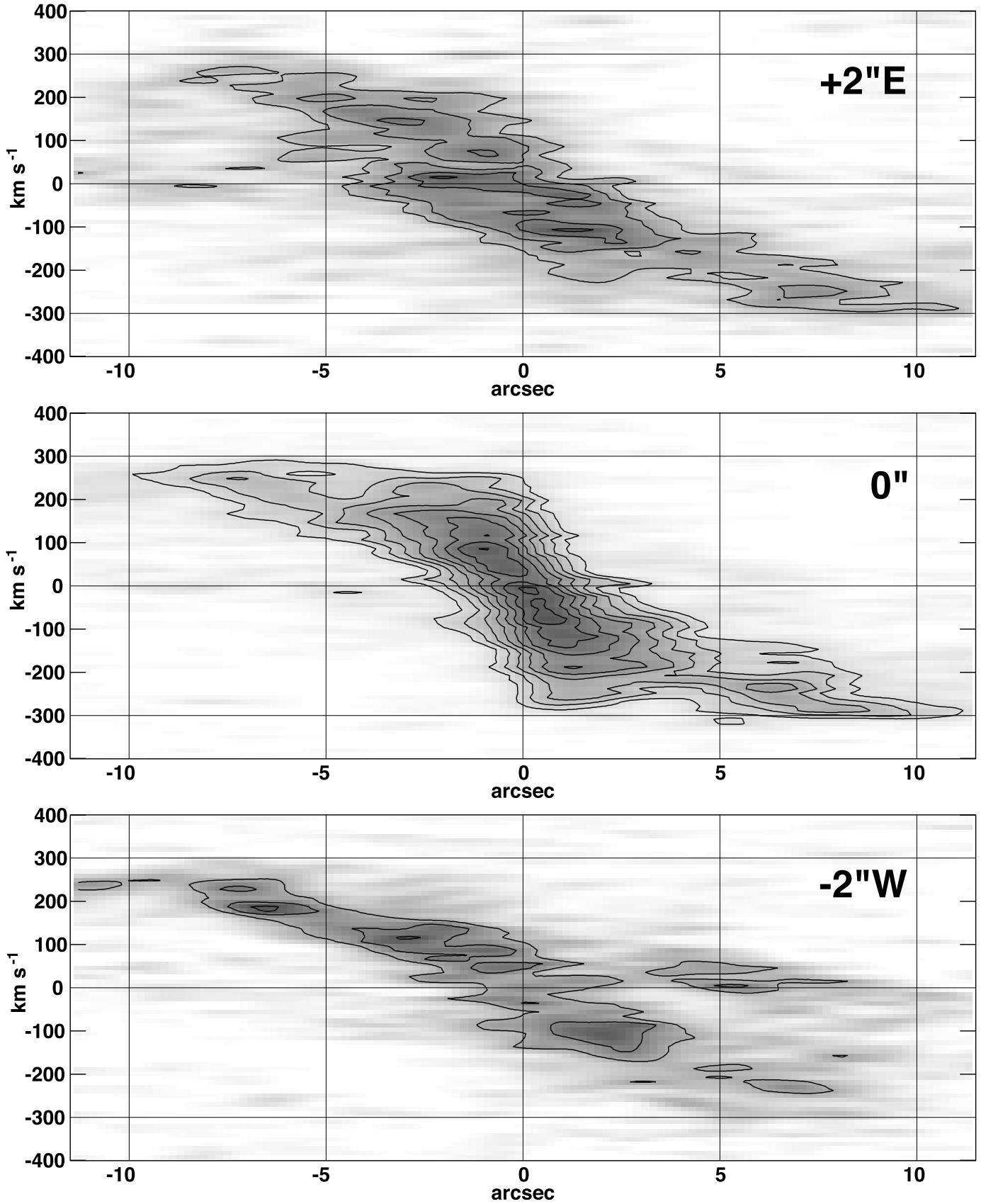

FIG. 10.— PV diagrams along the major axis (P.A. = 165 °) with offsets along the minor axis of $+2''$, $0''$ and $-2''$ ("+" denotes east). The slit-widths are $1''$. The axes are labeled relative to the dynamical center and systemic recession velocity (Table 3). Velocities have been corrected for inclination (77 °). Contours in all the panels are at 2, 3, 4, 5, 6, 7, 8, 9, 10 times 4.0×10^{-2} Jy beam^{-1}.

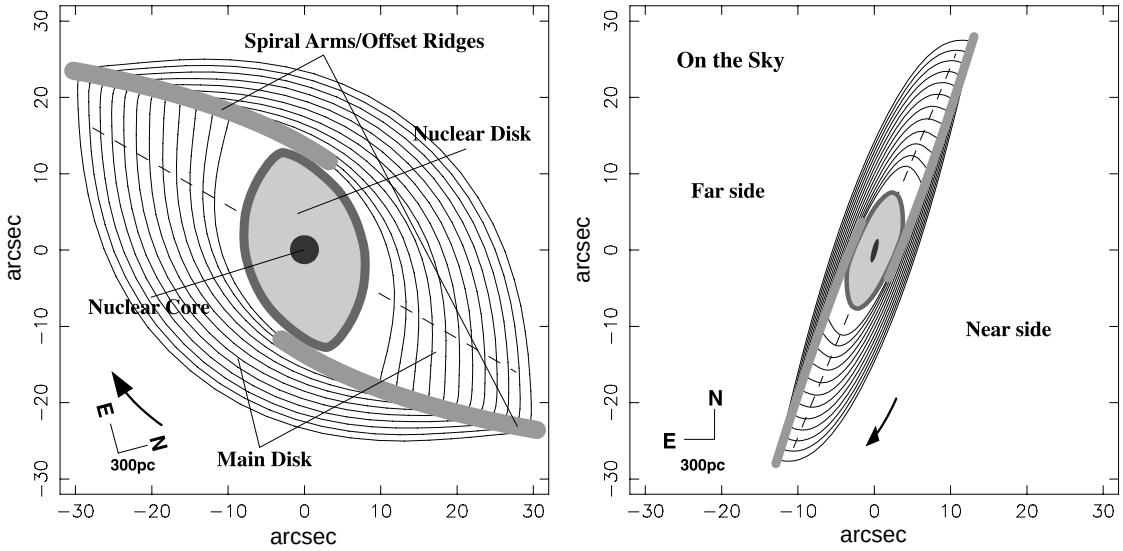

FIG. 11.— Schematic views of our interpretation of the molecular disk in NGC 3079. Four distinct components, the main disk, spiral arms/offset ridges, nuclear disk, and nuclear core, are drawn on the streamlines of our model orbits in the bar reference frame (§4.1). The bar has the position angle of 135 ° intrinsic to the galaxy from the north. *Left:* Face-on view. The galaxy major axis lies horizontally, while the bar runs along dashed line which is inclined clockwise by 30 ° from the horizontal. *Right:* Projection on the sky for P.A. = 165 ° and $i = 77°$.

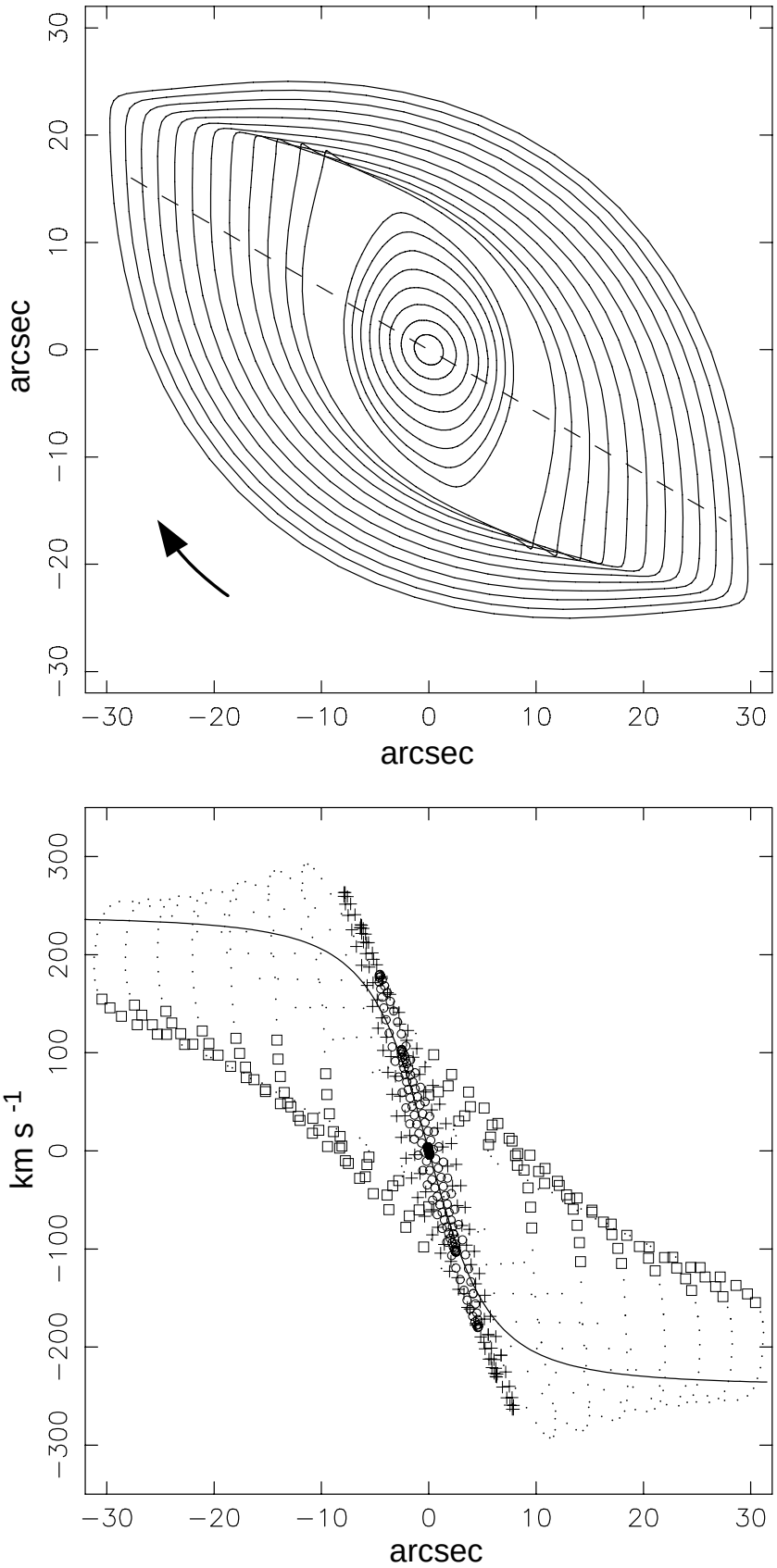

FIG. 12.— Model gas motions in the molecular disk of NGC 3079. *Top:* Face-on view of model orbits in a weak bar potential, on the frame rotating with the bar. The galaxy major axis runs horizontally. The bar is rotating clockwise, and runs along the dashed line (inclined from the horizontal by 30°). The orbits are calculated using a damped orbit model (Wada 1994). The inner and outer ILR and corotation occur at the radii of 8″, 11″ and 57″ (1″ = 76 pc) respectively. *Bottom:* Model PV diagram, which cuts the model galaxy along the galaxy major axis, with the width containing the full region at the top panel. The solid line shows the circular rotation curve. Different symbols are used for different orbits: circles are x_1-orbits inside the inner ILR, crosses are x_2-orbits, squares are x_1-orbits outside the outer ILR in front of the sharp turns on the streamlines, and dots are also the x_1-orbits at the rests.

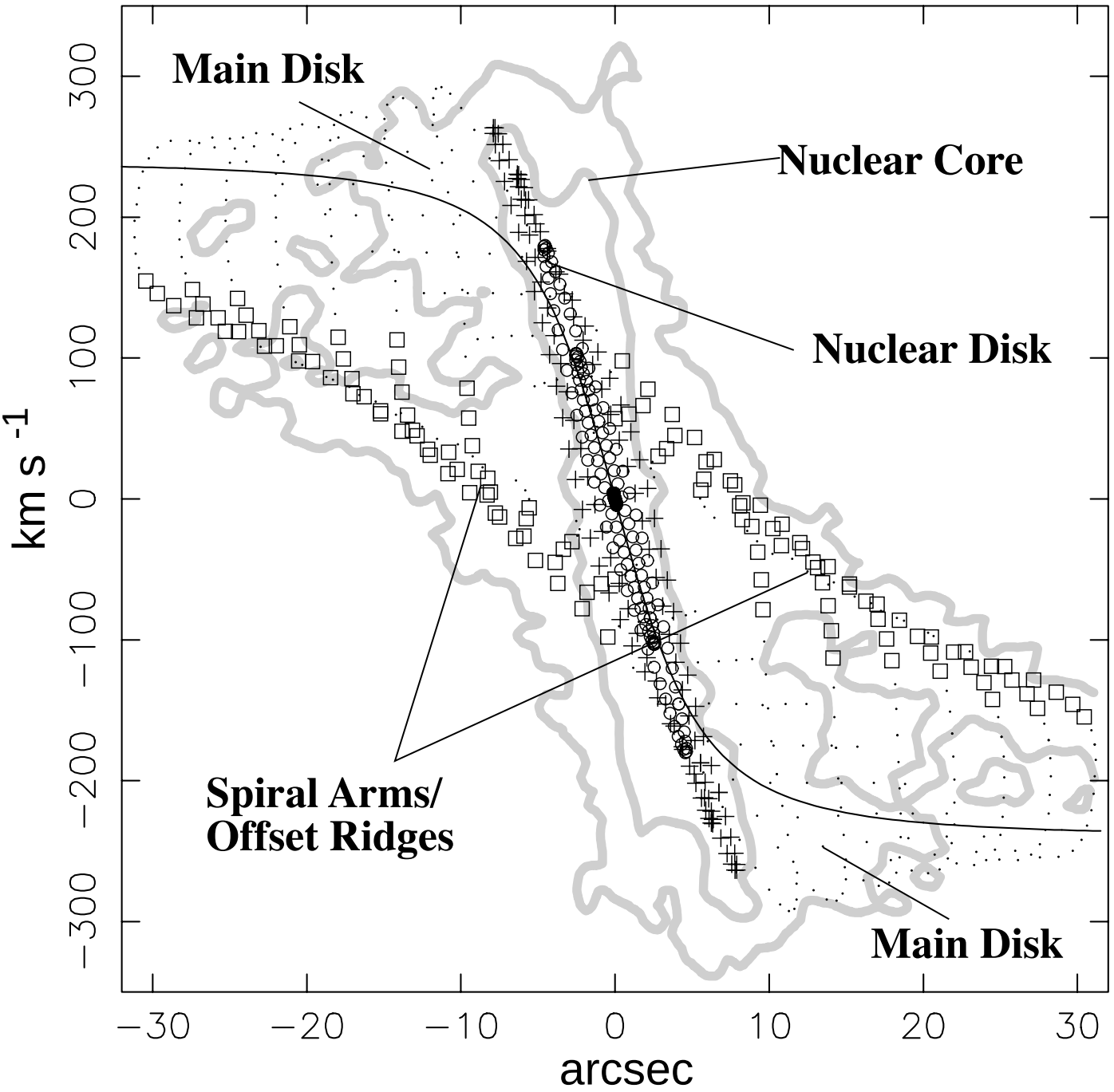

FIG. 13.— Comparison of the model and observed PV diagrams. Contours trace the observed PV diagram (Figure 4) at 8 and 40% of the peak intensity. Symbols plotted are the same as those in the bottom panel of Figure 12. Our model successfully reproduces the main features of the molecular disk of NGC 3079 except the nuclear core. This indicates the presence of a massive core.

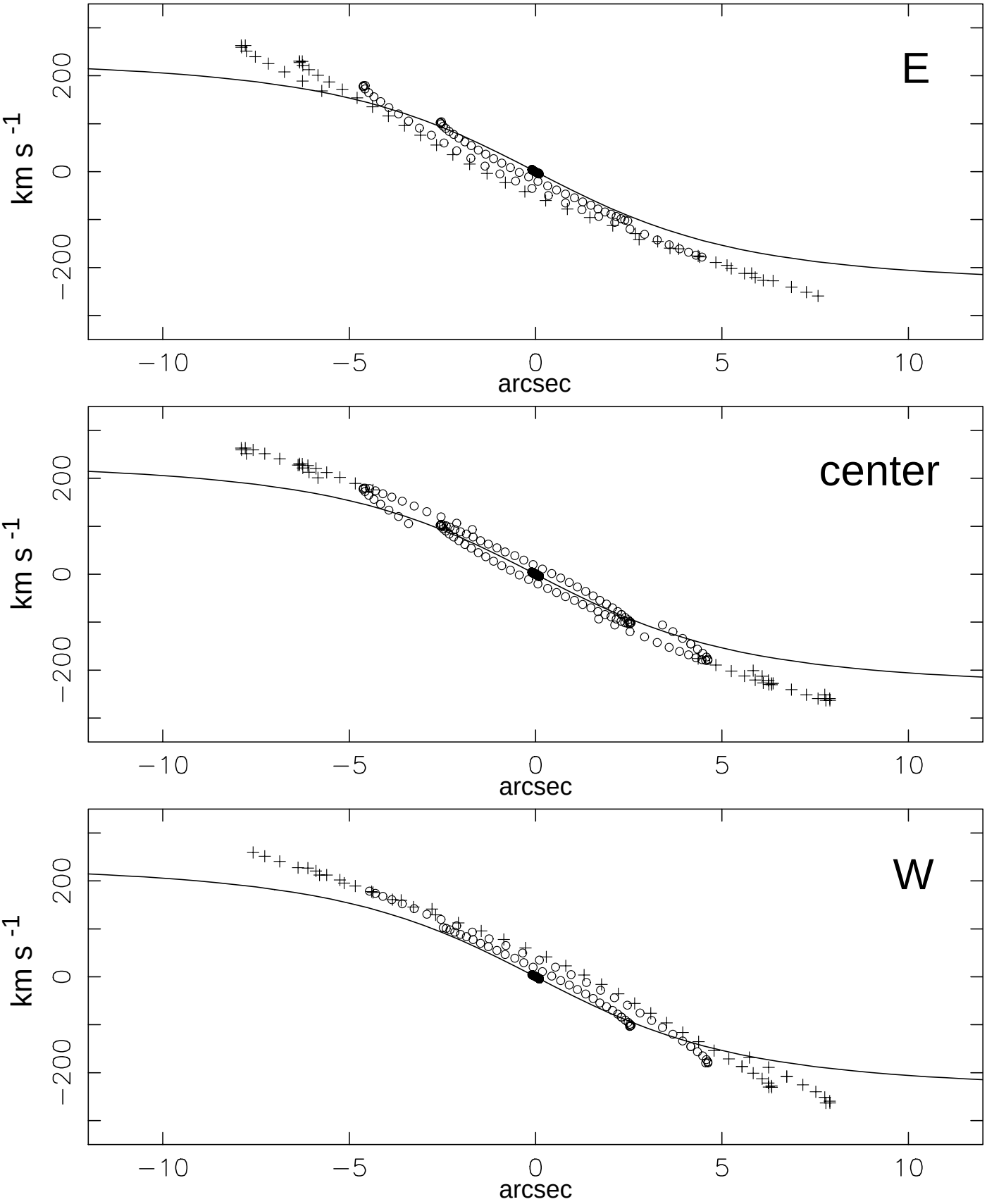

FIG. 14.— Model PV diagrams for the orbits within the outer ILR. The diagrams are cut along the major axis for east ($y > 0$ ″), center and west ($y < 0$″) sides, where y is the vertical axis on Figure 12 (*left*). The cut is 10 ″ width on the galaxy's face-on plane. The symbols are the same as those in Figure 12: crosses are x_2-orbits, and circles are x_1-orbits inside the inner ILR. The model well represents the bends (east and west) and twist (center) discussed in §3.3 (see Figure 10).

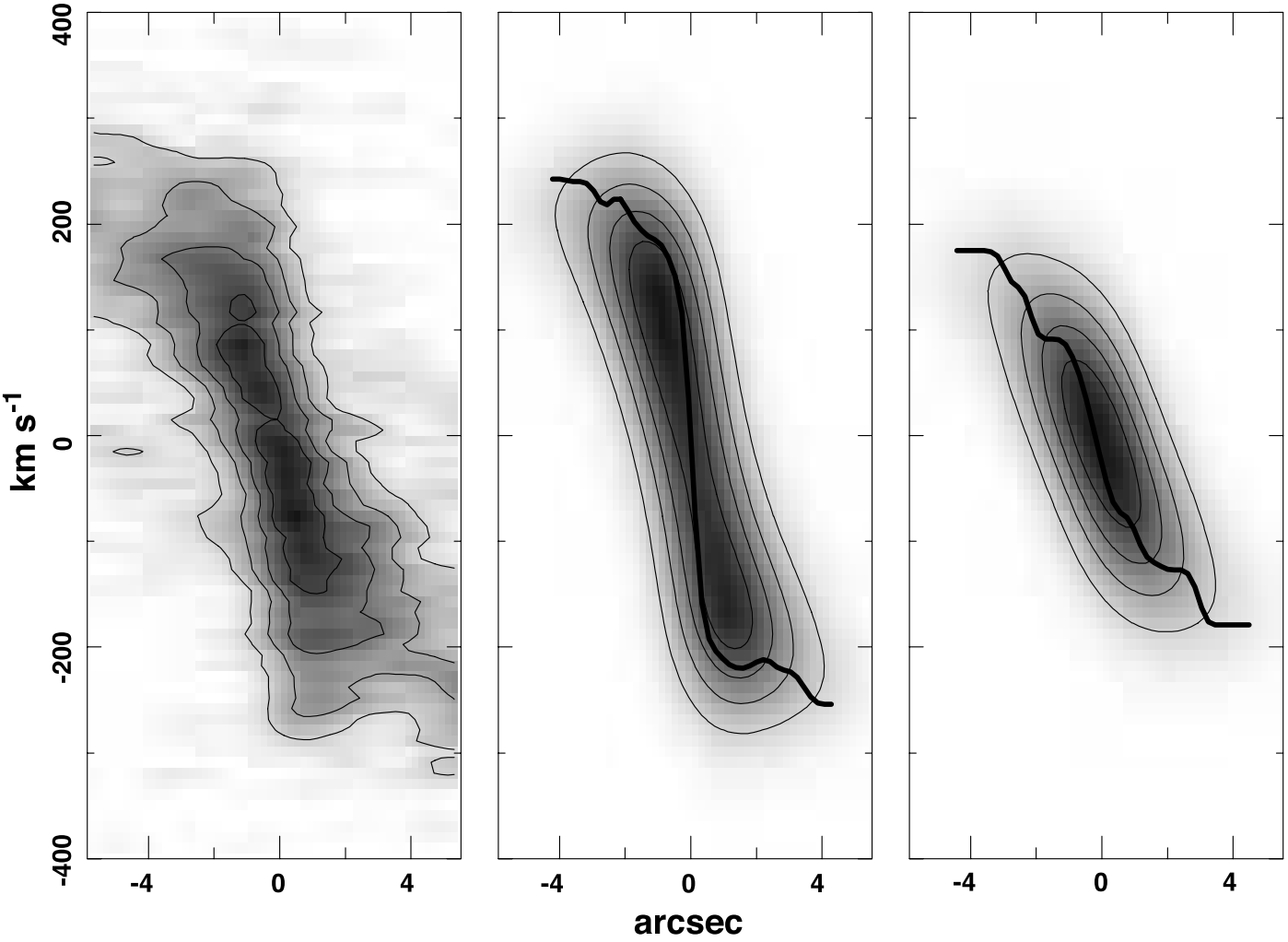

FIG. 15.— PV diagrams and rotation curves. The slit is 1″ wide. Contours are 20, 40, 60, 80% of the peak intensity in each panel. *Left:* Observed PV diagram in the central region of NGC 3079. *Middle:* PV diagram and rotation curve derived in the Takamiya & Sofue method. *Right:* PV diagram and rotation curve derived in the peak-tracing method.